

Deuterium retention and removal in liquid lithium determined by in situ NRA in Magnum-PSI

Citation for published version (APA):

Ou, W., Arnoldbik, W. M., Li, K., Rindt, P., & Morgan, T. W. (2022). Deuterium retention and removal in liquid lithium determined by in situ NRA in Magnum-PSI. *Nuclear Fusion*, 62(7), Article 076010. <https://doi.org/10.1088/1741-4326/ac3295>

Document license:
TAVERNE

DOI:
[10.1088/1741-4326/ac3295](https://doi.org/10.1088/1741-4326/ac3295)

Document status and date:
Published: 01/07/2022

Document Version:
Publisher's PDF, also known as Version of Record (includes final page, issue and volume numbers)

Please check the document version of this publication:

- A submitted manuscript is the version of the article upon submission and before peer-review. There can be important differences between the submitted version and the official published version of record. People interested in the research are advised to contact the author for the final version of the publication, or visit the DOI to the publisher's website.
- The final author version and the galley proof are versions of the publication after peer review.
- The final published version features the final layout of the paper including the volume, issue and page numbers.

[Link to publication](#)

General rights

Copyright and moral rights for the publications made accessible in the public portal are retained by the authors and/or other copyright owners and it is a condition of accessing publications that users recognise and abide by the legal requirements associated with these rights.

- Users may download and print one copy of any publication from the public portal for the purpose of private study or research.
- You may not further distribute the material or use it for any profit-making activity or commercial gain
- You may freely distribute the URL identifying the publication in the public portal.

If the publication is distributed under the terms of Article 25fa of the Dutch Copyright Act, indicated by the "Taverne" license above, please follow below link for the End User Agreement:

www.tue.nl/taverne

Take down policy

If you believe that this document breaches copyright please contact us at:

openaccess@tue.nl

providing details and we will investigate your claim.

PAPER

Deuterium retention and removal in liquid lithium determined by *in situ* NRA in Magnum-PSI

To cite this article: W. Ou *et al* 2022 *Nucl. Fusion* **62** 076010

View the [article online](#) for updates and enhancements.

You may also like

- [In situ nuclear reaction analysis of D retention in undamaged and self-damaged tungsten under atomic D exposure](#)
S Markelj, O V Ogorodnikova, P Pelicon et al.
- [Displacement damage stabilization by hydrogen presence under simultaneous W ion damage and D ion exposure](#)
S. Markelj, T. Schwarz-Selinger, M. Peovnik et al.
- [Deuterium retention in tungsten irradiated by different ions](#)
B. Wielunska, M. Mayer, T. Schwarz-Selinger et al.

Deuterium retention and removal in liquid lithium determined by *in situ* NRA in Magnum-PSI

W. Ou¹, W.M. Arnoldbik¹, K. Li², P. Rindt³ and T.W. Morgan^{1,3,*}

¹ DIFFER—Dutch Institute for Fundamental Energy Research, De Zaale 20, 5612 AJ Eindhoven, Netherlands

² Engineering Thermophysics, Chinese Academy of Science, Beijing 100190, China

³ Science and Technology of Nuclear Fusion Group, Eindhoven University of Technology, Eindhoven, Netherlands

E-mail: T.W.Morgan@diffier.nl

Received 22 July 2021, revised 5 October 2021

Accepted for publication 22 October 2021

Published 26 April 2022




CrossMark

Abstract

In this work, Li-filled 3D-printed porous tungsten samples were exposed to deuterium (D) plasma in Magnum-PSI with a wide ion flux from 4×10^{22} to $1.5 \times 10^{24} \text{ m}^{-2} \text{ s}^{-1}$ and with a corresponding wide temperature range from below Li melting point (180.5 °C) to above Li deuteride (LiD) melting point (~ 690 °C). The formation, decomposition and melting of LiD have been directly observed in the experiment via infra-red thermometry and visually post-mortem while still in vacuo, and correlated to the D retained content. The LiD formation was characterized by a solid precipitate layer formed on the surface with high emissivity (0.6–0.9) characterized by a blue or dark blue color after exposure. The melting of Li–LiD layer was found to occur close to the temperature predicted by Li–LiD phase diagram. *In situ* nuclear reaction analysis (NRA) was applied to perform the measurement of D retained in Li samples immediately after exposure without breaking the vacuum. D depth profiles were determined by NRA, in which the highest D concentration (15–45 at.%) was found in the top several micrometers and decreases with depth to low levels (<5%) within 5–30 μm . No pure LiD layer was found on the sample surfaces, however a D concentration close to 50 at.% was observed on a Li–D co-deposited layer on the clamping ring in some cases. The experiments also indicate that the D retained increases with increasing temperature until ~ 500 °C. At temperatures beyond ~ 500 °C the dissociation of LiD starts to dominate and the deuterium retention started to decrease. Overall, D retained fraction for all cases was found to be below $\sim 2\%$, which is significantly different from literatures where full uptake has been suggested. A 1D reaction–diffusion (RD) model based on D diffusion and chemical reactions with Li has been built. D depth profiles from the RD modelling can roughly match that from NRA measurement and a low D retained fraction below $\sim 2\%$ was also indicated by the model. The model can also help explain the relationship between D retained and the surface temperature and fluence. After D plasma exposure, either helium or H plasma was utilized to remove the retained D in Li and both were proved to be effective and the removal efficiency can be as high as 96% above 420 °C.

Keywords: lithium, deuterium retention, *in situ* nuclear reaction analysis

* Author to whom any correspondence should be addressed.

 Supplementary material for this article is available [online](#)

(Some figures may appear in colour only in the online journal)

1. Introduction

One of the biggest challenges for a fusion reactor based on magnetic confinement is to dissipate extremely high heat and particle fluxes in the divertor area [1–3]. Conventional solid plasma-facing materials (PFMs) such as tungsten could suffer from cracking, blistering and even melting under transient loadings and will also suffer from radiation damage due to high neutron loading as a consequence of the fusion reactions [4–7]. One possible alternative solution is to use liquid metals (LMs) as a PFM in the divertor region [8–14]. Owing to their liquid nature, LMs can avoid much of the degradation in performance caused by neutron radiation and quickly refresh and self-heal via flow. Their evaporation and radiation can significantly lower the coming heat flux and by forming a vapor cloud in front of them can provide vapor shielding for the liquid bulk, thus can protect the underlying solid substrate from extreme conditions in the fusion reactor [10, 15–17].

Among LMs, lithium (Li) has been proposed as one of most promising liquid PFMs and is historically the most widely studied [8, 9, 12, 13, 18]. As the lightest metal, Li has a low Z ($Z = 3$) and its content can be highly tolerated in fusion core plasma. Owing to its high affinity with hydrogen isotopes (HI), the use of Li as a PFM can lower HI recycling rate and significantly improve plasma performance, which has been demonstrated in TFTR [19, 20], CDX-U [21], LTX [22], EAST [17, 23, 24] and NSTX [15, 25], amongst other devices [26]. However, due to safety issues arising from the radioactivity of tritium (T) and the fact that tritium is a scarce fusion fuel which must be generated in the reactor itself, it is required that tritium inventory in PFMs should be as low as possible. For example, the inventory level of tritium in ITER is limited below 700 g [27]. This suggests that this would be a critical issue for the use of Li in fusion reactors, and for this reason alternative LMs such as Sn may be preferred as the trapping of HI in pure Sn is extremely low [28–31]. If tritium retention is too high, alternatively a flowing Li system where T is removed elsewhere should be employed. Such a system could offer a continuously low-recycling surface which could have advantages, but would be complex to achieve [26].

By using deuterium (D) as a proxy of tritium, a full uptake of D in Li under D plasma at a flux up to $4 \times 10^{22} \text{ m}^{-2} \text{ s}^{-1}$ has been determined by Baldwin *et al* and the retention fraction was found to be independent of temperature over their explored range (250–400 °C) [32]. They proposed the high D retention was due to the combination of D atoms with Li to form lithium deuteride (LiD), which remains solid until 690 °C. A trapping efficiency as high as 97% was also observed by Erents using 18 keV D ions, but was found to decrease

at 407 °C until it fell towards zero above 427 °C [25]. The decrease in trapping efficiency was suggested as being due to the dissociation of LiD. In the experiments on the T-11M tokamak with a lithium limiter [14], Mirnov *et al* have found that deuterium could be release at temperature higher than 320 °C, and a surface temperature of 400–500 °C was suggested for a Li plasma-facing component (PFC) to minimize tritium inventory. Additionally Oyarzabal *et al* have reported a desorption peak at ~ 500 °C for Li exposed to and saturated with H/D, which was well below the expected thermal decomposition temperature [33, 34]. While, using Li films, Capece *et al* observed the formation of LiD films after Li exposure to D ion beam and D retention was found to decrease with the increasing temperature and a release peak at 390 °C was also spotted for the LiD film [35]. Recently, in [36] Castro *et al* have found that HI retention in lithium can be significantly reduced at the surface with high temperature. All together these results suggest that operation at higher temperatures ($> \sim 500$ °C) may prevent the strong trapping of HI in Li. Newer concepts such as the vapor-box divertor [37] which utilizes Li vapor to reduce heat loads at the PFCs implicitly rely on this assumption to prevent excessive tritium inventory build-up. Therefore, a full understanding of tritium retention in Li under fusion-relevant flux plasmas is vital for its application as a PFM in fusion reactors.

Data on HI retention in Li under fusion-relevant plasma conditions, which are typically with high fluxes ($10^{23-25} \text{ m}^{-2} \text{ s}^{-1}$) and wide temperature range (300–800 °C), is scarce and the influence of temperature and flux/fluence on the retention is not fully understood. What's more, Li is highly reactive when exposed to atmospheric gases, resulting in fast oxidation, nitridation and reactions with water vapor. If samples are removed from vacuum conditions, LiH/D/T itself can also react with water vapor and release $\text{H}_2/\text{D}_2/\text{T}_2$ gas. These effects could have a significant influence on the measurement of HI retention and desorption. Lastly little exploration has been made of techniques which could be applied to reduce the HI inventory in lithium *in situ*. In this work we aimed to explore this fusion relevant parameter range while avoiding atmospheric contamination. Therefore, we exposed Li-filled samples to high flux ($10^{23-24} \text{ m}^{-2} \text{ s}^{-1}$) D plasma in Magnum-PSI [30, 38, 39], leading to a surface temperature variation from Li melting point (180.5 °C) to LiD melting point (690 °C). *In situ* nuclear reaction analysis (NRA) was then performed immediately after exposure without breaking the vacuum, in which we can directly get insights into D depth profiles in Li. After this measurement we then applied a second plasma treatment in Magnum-PSI with either He or H plasma and then measured again with NRA to determine the amount of D that was removed.

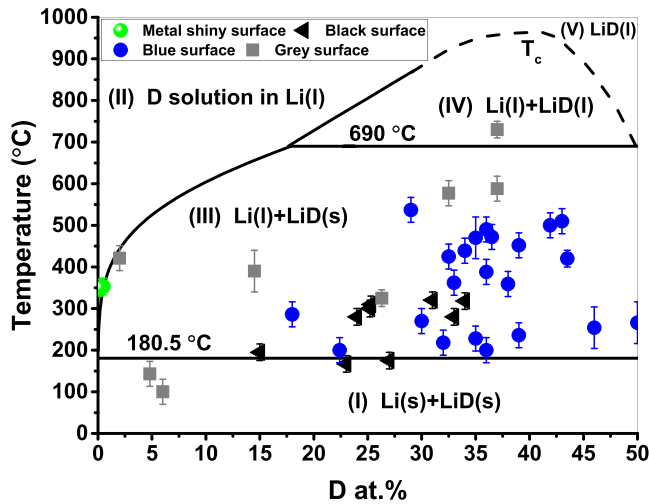


Figure 1. Phase diagram for Li–LiD system. The dashed line is the predicted closure that remains to be verified experimentally. The scattered points are the experimental data deduced from NRA measurement which refers to section 4, and divided into 4 groups according to different surface appearance of the positions shown in figure 6(b), namely metal shiny, grey, black and blue.

2. Theory

2.1. Phase diagram for Li–LiD system

To gain insights into deuterium retention in lithium, a first understanding of the Li–LiD phase diagram is needed, which is illustrated in figure 1 following [40–44]. The phase diagram is displayed as a function of temperature and deuterium atomic fraction, and mainly consists of five regions as described below.

- (I) Both Li and LiD are present as solids at temperature below Li melting point (~ 180.5 °C);
- (II) The region is a deuterium solution of liquid lithium, where deuterium concentration is below its solubility limit that can be described by equation (1) as below [40, 42]. The equation offers a liquidus line to separate regions (II) and (III).

$$x_D \text{ (mol frac \%)} = 10^{4.321 - \frac{2873}{T}} \quad (1)$$

- (III) At temperatures between the Li melting point to the LiD melting point (~ 690 °C), depending on D concentration a biphasic liquid lithium containing solid LiD is presented. If solid LiD precipitation does not take place, a colloidal suspension of nano and micro LiD particles can be formed and the diphasic can be stable.
- (IV) A coexisting liquid phase of lithium and LiD can be found when temperature is beyond 690 °C but below the critical temperature (~ 956 °C);
- (V) This region is a homogeneous melt, where Li and LiD are miscible in all proportions.

At high temperature LiD can decompose, depending on deuterium partial pressure. The decomposition pressure of LiD can be expressed by [32, 45]:

$$P_{\text{decomp}} \text{ (Pa)} = 10^{-3} \cdot e^{(39.93 - 23590/T)}, \quad (2)$$

where T is the temperature in Kelvin. When the decomposition pressure is equal to the surrounding deuterium pressure, an equilibrium could be built between LiD dissociation and formation.

Figure 1 implies that in order to ensure a liquid surface that can continuously self-refresh and self-heal, D supply to the Li should be limited to keep its concentration below the solubility limit, or the target needs to be heated above 690 °C, at which point the solid LiD could melt and decompose very fast due to a very high decomposition pressure (~ 5000 Pa).

2.2. Deuterium diffusion coefficient and surface recombination for Li–LiD system

Deuterium diffusion and surface recombination are two key points for the processes of D retention and reemission. As no reliable experimental data on D diffusion coefficient in pure liquid Li is available, here we take an approximation from Moriyama’s experiment where the temperature dependence of tritium diffusion coefficient in very dilute liquid lithium was measured [46]. In deuterium environment, with the formation of LiD in Li, D diffusivity in Li could change. By using first-principle, Chen *et al* have given some D diffusivity values in Li–LiD system with different LiD concentration [47]. These results were used by Abrams in [48].

An expression for HI surface recombination coefficient on metallic surface has been deduced by Pick and Baldwin [43, 49] and is given as below

$$k_r \text{ (m}^4 \text{ s}^{-1}\text{)} = 2.63 \times 10^{24} \cdot \kappa_0^{-2} \cdot \sigma \cdot (2MT)^{-1/2} \cdot e^{2(E_s - E_c)/(kT)}, \quad (3)$$

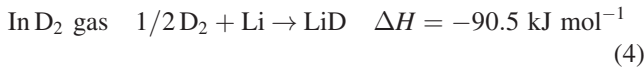
where κ_0 is the pre-factor in Sieverts’ constant, σ a constant related to surface-site availability, M the atomic mass in u of the desorbing species, E_s the enthalpy of solution, E_c is activation energy of for chemisorption and k is Boltzmann constant. For an ideally clean surface, σ can be taken to be unity and E_c is reduced to zero.

In Baldwin’s experiment [43], $\sigma = 0.01$ and $E_c = 0.1$ eV were taken for the liquid lithium surface with LiD ‘impurity’. This work suggested that D desorption from a Li surface is recombination-limited, firstly due to LiD presence but also due to its high reactivity such that the Li surface is natively contaminated by either oxide or other impurities. During plasma exposure, an ‘ideally’ clean surface of liquid lithium could be achieved due to plasma cleaning or self-refreshing. In this case, $\sigma = 1$ and $E_c = 0$ eV can be applied, which can reach a high surface recombination that is 3–4 orders of magnitude higher than that of the Li–LiD surface. If an ‘ideally’ clean surface is assumed, D desorption from Li surface could shift to a diffusion-limited regime, resulting into a low D retention. The validity of these assumptions is explored below.

2.3. One-dimensional reaction–diffusion (1D RD) model for D atoms interacting with Li

Due to the high reactivity of Li, it can chemically combine with both deuterium gas and deuterium atoms to form LiD, which

can be described by the reactions below:



Compared to D₂ molecules D atoms are more active to Li, thus in a D plasma atmosphere, as in our experiment, we will mainly take the reaction equation (5) into account. In the reaction equation (5), the depletion rate of pure Li atoms and the formation rate of LiD molecules can be expressed by

$$-\frac{dn_{\text{Li}}}{dt} = \frac{dn_{\text{LiD}}}{dt} = kn_{\text{D}}n_{\text{Li}}, \quad (6)$$

where n_{Li} and n_{LiD} are the number density (atoms/m⁻³) of pure Li atoms and LiD molecules, respectively, and n_{D} is the mobile/free D atom density in Li (i.e. not including D atoms existing in the form of LiD) where k (m³ s⁻¹) = $Ae^{-E_a/RT}$ is defined as the reaction rate constant and E_a is the activation energy, A the pre-exponential factor, R the gas constant and T temperature in Kelvin.

To estimate the reaction rate constant k , a simple case is proposed, in which liquid convection and volume change due to LiD formation are ignored and it is assumed that $d(n_{\text{Li}} + n_{\text{LiD}})/dt = 0$. Considering that the top Li layer is implanted by D ions, and with the formation of LiD the diffusion coefficient of D in LiD becomes much smaller than that in pure liquid Li, we assume the boundary condition is diffusion-limited and the implanted D atom concentration can be estimated by [31, 50]:

$$n_{\text{D}} \approx \frac{\Gamma_i \cdot r_{\text{impl}}}{D(f)}, \quad (7)$$

where Γ_i is deuterium plasma ion flux and r_{impl} is the deuterium ion implantation range and around 1.3 nm for 5 eV D⁺ according to TRIM simulation; $D(f)$ is the deuterium diffusivity in Li–LiD phase and is a function of $f = n_{\text{LiD}}/n_{\text{Li}}$, which can be taken from [47].

After D ions are implanted into Li in the form of atoms (or D atoms directly diffuse from the surface into Li), on the one hand, a part of these D atoms will chemically combine with Li atoms to form LiD; on the other hand, the residual D atoms will continue to diffuse deeper following the n_{D} concentration gradient. The temperature in the top tens of micrometers of Li samples can be assumed uniform. Thus, the mobile/dynamic deuterium concentration in bulk Li targets can be expressed as below according to Fick's second diffusion law by adding a reaction term.

$$\frac{\partial n_{\text{D}}(x, t)}{\partial t} = \frac{\partial}{\partial x} \left[D(f) \cdot \frac{\partial n_{\text{D}}}{\partial x} \right] - k \cdot n_{\text{D}} \cdot n_{\text{Li}}. \quad (8)$$

From equation (6), we have

$$-\frac{\partial n_{\text{Li}}(x, t)}{\partial t} = kn_{\text{D}}n_{\text{Li}}. \quad (9)$$

Equations (8) and (9) can be used to model deuterium diffusion and reaction in Li, and thus further to predict deuterium

inventory. Both n_{D} and n_{Li} are a function of time (t) and lithium depth (x). The initial and boundary conditions for $n_{\text{D}}(x, t)$ and $n_{\text{Li}}(x, t)$ in Li target with a thickness of L (m) can be set as below.

$$\text{Initial condition: } n_{\text{D}}(x, 0) = 0 \text{ atoms/m}^3; n_{\text{Li}}(x, 0) = n_0;$$

$$\text{Boundary condition: } n_{\text{D}}(0, t) = \frac{\Gamma_i r_{\text{impl}}}{D},$$

$$n_{\text{D}}(L, t) = 0 \text{ atoms/m}^3;$$

$$n_{\text{Li}}(0, t) = n_0 \times e^{-kt \frac{\Gamma_i r_{\text{impl}}}{D}}; n_{\text{Li}}(L, 0) = n_0,$$

where $n_0 \approx 4.4 \times 10^{28}$ atoms/m³ is the number density of static liquid lithium.

It can be foreseen that when Li is exposed to D plasma, Li atoms in top layer will first combine with the incoming D atoms to form solid LiD assuming that a high D ion flux is provided, leading to a high D concentration near the surface. This was observed in [51]. As the D diffusivity decreases with D concentration, the deeper the layer, the more difficult for D diffusing, which would lead to a D concentration gradient from the surface to deep Li layer. Only given enough time for the chemical reaction of equation (5), is it possible to form a uniform LiD bulk target. Some similar behaviors have been observed in [52], where the reaction rate of hydrogen gas with lithium was found to be initially proportional to the mass of lithium and the hydrogen pressure, then to fall off and become diffusion-controlled. While if the D ion flux is low enough and the Li surface is also 'ideally' clean to ensure a high surface recombination according to equation (1), D concentration would be expected to be below its solubility and there is no LiD formation. It should be noted that the 1D RD model does not take LiD decomposition into account. At high temperature, the decomposition pressure of LiD can be beyond the surrounding deuterium partial pressure resulting into LiD dissociation. In this case, a regime of LiD formation competing with its dissociation might exist.

A first sign of LiD formation can be judged from its appearance. Both pure LiD and LiH are colorless solid, while normally commercial samples are white to grey. However, during synthesis processes large crystals can be grown, which have the appearance of bluish or coal-black color. This is because of the presence of colloidal lithium [53, 54]. Thus, during experiments the appearance of Li sample surface can be observed to judge if LiD forms or not.

3. Experimental details

3.1. Achievement of in situ IBA analysis on Magnum-PSI

Magnum-PSI is a fusion-relevant linear plasma device capable of achieving plasma flux and fluence as high as 10^{23-25} m⁻² s⁻¹ and 10^{26-30} m⁻² [39, 55, 56] and due to its strong magnetic field confinement and differential pumping system the ion fraction is above 95% [57]. The DIFFER ion beam facility (IBF) was built to directly connect to the target exchange and analysis chamber (TEAC) of Magnum-PSI making it possible to

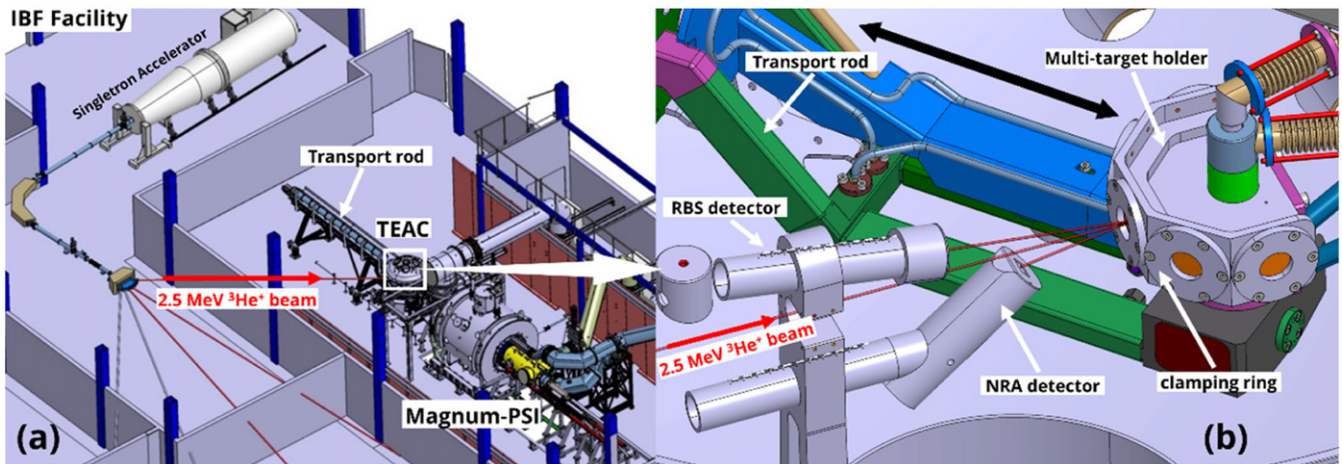


Figure 2. (a) Schematic diagram of IBF and Magnum-PSI; (b) target and IBA system in the TEAC. The ion beam is transported by means of magnetic elements from the Singletron to the TEAC, where simultaneously NRA and RBS are performed just before, or immediately after plasma exposure in Magnum-PSI without breaking the vacuum. The multi-target holder was used in this experiment, which can be moved forward and back by the transport rod following the direction of double black arrow.

perform ion beam analysis (IBA), such as NRA and Rutherford backscattering spectrometry (RBS), on targets immediately before or after plasma exposure in Magnum-PSI without breaking the vacuum. A schematic diagram of the IBA setup at Magnum-PSI can be seen in figure 2. The IBF uses a 3.5 MV Singletron ion accelerator where RF-plasma generated ions such as $^3\text{He}^+$ and $^4\text{He}^+$ are electrostatically accelerated to the required energy and then transported to the target position in the TEAC. Five samples can be mounted on Magnum-PSI's multi-target holder (figure 2(b)), of which four of them can be directly bombarded by the ion beam. As seen in figure 2(b), both RBS and NRA detectors were installed in the TEAC to register energy spectra from particles scatter from the target (RBS) or are created by a nuclear reaction (NRA) in the target. The ion beam hits the target at perpendicular incidence.

In this experiment the applied ion beam was $2.5\text{ MeV } ^3\text{He}^+$ beam with a spot area of $\sim 2 \times 4\text{ mm}^2$. The nuclear reaction $\text{D}(^3\text{He}, \text{p})^4\text{He}$ was used to determine deuterium concentration in the top layer (probing depth is $\sim 32\text{ }\mu\text{m}$ for $2.5\text{ MeV } ^3\text{He}^+$ bombarding pure Li) of Li samples. In order to prevent backscattered ^3He ions reaching the NRA detector, a $15\text{ }\mu\text{m}$ thick Kapton ($\text{H}_{10}\text{C}_{22}\text{N}_2\text{O}_5$) was placed in front of the NRA detector. The reaction angle for NRA (detector under the ion beam) was $168^\circ\text{--}171.5^\circ$ and the scattering angle was $166.0^\circ\text{--}169.0^\circ$ for RBS (detector above the ion beam). The exact angles depend on the position of the beam spots on the target surface and are taken into account for the data-analysis. For deuterium a calibration sample has been used and the systematic error is estimated to be 7%.

3.2. Sample preparation and 3D-printed tungsten targets

Li-filled 3D-printed tungsten targets [58], forming a capillary-porous system (CPS) [59], were used in this experiment. Figure 3(a) shows an empty 3D-printed tungsten target with a diameter of 24.5 mm and a height of 17 mm and (b) displays its surface texture consisted of micro-blocks separated by

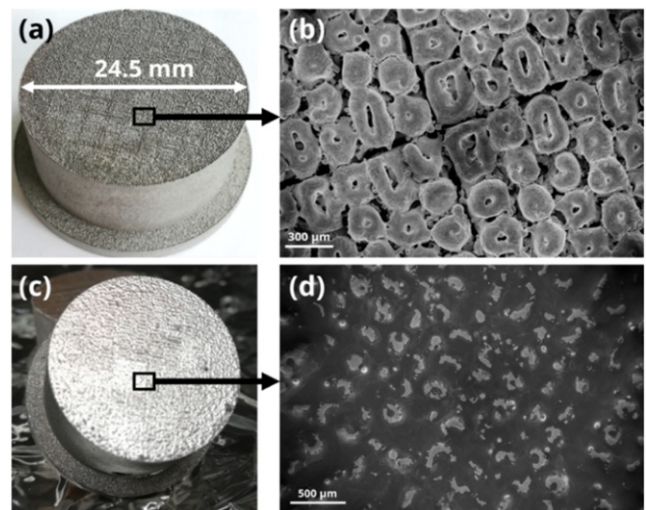


Figure 3. 3D-printed tungsten sample (a) before Li filling and (c) after Li filling; a SEM of the sample surface (b) before Li filling and (d) after Li filling.

micro-trenches, whose designed size was $\sim 100\text{ }\mu\text{m}$. This texture stabilizes the liquid by surface tension. The 3D-printed tungsten target can provide a continuous liquid surface via inner wicking channels from an internal reservoir, in which lithium can be pre-filled. More information about the design of 3D-printed tungsten targets can be found in [58].

Prior to LM filling, the 3D-printed tungsten target was first cleaned in hot 37% HCl acid following by ultrasonic bath with acetone. Then the target was heated up to $1200\text{ }^\circ\text{C}$ for 1.5 h in vacuum oven at a background pressure of 10^{-5} Pa to remove oxides and other impurities. The lithium filling was carried out in a glovebox with argon atmosphere, in which both oxygen and water concentrations were controlled below 5 ppm. Figure 3(c) shows a photo of a Li-filled 3D-printed tungsten sample taken in the glovebox. A good wetting has been achieved after filling and a SEM of the Li-filled sample

Table 1. Plasma exposure conditions for all Li-filled 3D-printed tungsten samples.

Sample ID	#1	#2	#3	#4	#5	#6	#7	#8	#9
Γ_{iPeak} ($10^{23} \text{ m}^{-2} \text{ s}^{-1}$)	0.35	0.84	0.84	0.84	3.3	5.2	5.2	10.2	15.0
T_{peak} ($^{\circ}\text{C}$)	195	355	310	345	415	405	470	530	735
Time (s)	200	200	400	800	200	200	800	200	200
Φ_{peak} (10^{25} D m^{-2})	0.7	1.7	3.4	6.8	6.6	10.4	20.8	20.2	30.0
D removal shot	H	He	H	H	He	H	H	H	He
Γ_{iPeak} ($10^{23} \text{ m}^{-2} \text{ s}^{-1}$)	0.27	4.5	0.4	0.4	5.0	4.0	4.0	8.6	5.0
T_{peak} ($^{\circ}\text{C}$)	211	395	460	360	700	425	580	550	650

surface can be seen in figure 3(d). In total, 9 Li-filled 3D-printed tungsten samples were used in the experiment and numbered as #1 to #9, as seen in table 1. Each of them contained ~ 1.8 g lithium.

3.3. Diagnostics and plasma exposure in Magnum-PSI

3.3.1. Diagnostics. Plasma density (n_e) and temperature (T_e) profiles at a distance of 30 mm to the target exposure surface were measured by Thomson scattering (TS). This was performed on a molybdenum reference dummy with the same dimension as the 3D-printed tungsten target prior to the exposure of Li-filled 3D-printed tungsten samples in order to avoid potential lithium droplets entering the TS laser tube. The incident plasma ion flux on the target surface was determined from the Bohm criterion using n_e and T_e [56] and the applied peak D ion flux was in the range 3.5×10^{22} – $1.5 \times 10^{24} \text{ m}^{-2} \text{ s}^{-1}$ with Gaussian beam shape with a FWHM of 16–20 mm. All exposures were carried out under floating conditions. An Avantes spectrometer (Avantes AvaSpec-2048-USM2-RM) was focused on the target surface viewing at $\sim 45^{\circ}$ to normal in order to monitor plasma emission lines in the range of 299–950 nm, including emission lines from lithium and possible impurities. A Phantom V12 visible fast camera with Li I emission line (670.8 nm) filter was used viewing tangentially to the target surface in order to capture possible droplet ejection with a frame rate of 100–1000 Hz.

A single-chord multi-wavelength pyrometer and an infrared (IR) camera were used to acquire surface temperature evolution of the targets during exposure. The pyrometer (FAR SpectroPyrometer model FMPI) has a spot size on the target of $\sim 4 \times 6 \text{ mm}^2$ and operates in the wavelength range of 900–1700 nm. Because it measures the grey-body curve of the thermal emission it does not require prior knowledge of the surface emissivity, however it only operates when recording sufficient signal, which is typically above 500°C for low emissivity surfaces (< 0.2). The IR camera (FLIR SC7500MB) can measure low temperatures (5 – 300°C) in 2 – $5 \mu\text{m}$ range and high temperatures (300 – 2000°C) in 3.97 – $4.01 \mu\text{m}$ range. It was operated at full frame (320×256 pixels) at 380 Hz. The transmission of the window and the target surface emissivity are two key parameters to determine surface temperature for the IR camera. The transmission of window has been pre-determined to be 14.5% by an emissivity-known material combined with pyrometer. For the case of possible pollution of the window by lithium, the transmission was monitored by performing plasma shots on the molybdenum reference

dummy whose emissivity was known in the experiment. It was observed that during the whole experiment the window transmission did not significantly change and the error was below 5% due to this. The emissivity determination of the lithium sample surfaces was more complicated due to the formation of LiD and possible presence of impurities during target mounting as the emissivity is very sensitive to target surface compositions and the emissivity varies a lot for pure Li, oxidized Li and LiD-Li mixtures. To determine lithium sample surface emissivity either the IR temperature was matched at the same position with the temperature from the pyrometer when pyrometer data was available, or the plateau of temperature during the target cooling-down process after exposure was used if not. This plateau corresponds to the lithium melting point (180.5°C) and is caused by the phase transition. In this case, the emissivity of Li samples due to the formation of LiD under D plasma was determined in the range of 0.6–0.9, depending on the exact surface conditions compared to 0.1–0.15 for clean Li surfaces.

3.3.2. Li sample cleaning by He plasma. Li samples were sealed in a sample box with argon atmosphere to transport from glovebox to Magnum-PSI. However, oxidation of the Li surface was still inevitable during the target mounting process in the TEAC. To remove this oxide layer and other possible impurities, all Li samples were pre-exposed to helium (He) plasma. The He plasma cleaning shot lasted for 100 s for each sample and the peak particle flux and electron temperature of He plasma were around $5.0 \times 10^{23} \text{ m}^{-2} \text{ s}^{-1}$ and 0.9 eV, respectively. During the cleaning the surface temperature was around 300 – 400°C , except for Li sample #3, in which a temperature as high as 700 – 800°C was reached in the first 50 s possibly due to bad wetting of Li bulk with tungsten bottom or bad thermal conductivity between the sample and the sample holder. For this #3 sample, a thick pure Li deposited layer was presented on the clamping ring after He plasma cleaning due to strong evaporation and re-deposition (see Li sample #3 in figure 6(b)). A typical time-evolution of surface temperature from the cleaning shot can be seen in figure 5(a), in which the emissivity 0.1 was used for pure liquid lithium after the impurity layer was removed [60, 61]. The removal of the impurities can also clearly be seen in supplementary video S-1 (<https://stacks.iop.org/NF/62/076010/mmedia>). Combined with the video taken by Phantom fast camera (see supplementary video S-2), three main mechanisms attributed to the removal of impurities are proposed: (1) breaking down of the solid impurity layer, which has a high

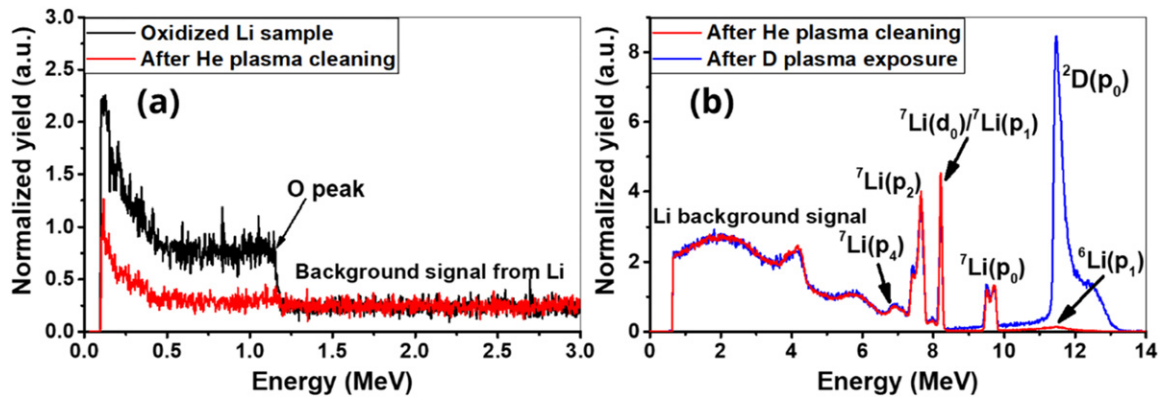


Figure 4. (a) RBS spectrum of oxidized Li and He plasma-cleaned Li; (b) NRA spectrum of He plasma-cleaned Li and D plasma-exposed Li. The smooth Li background feature is mainly composed by the nuclear reactions ${}^7\text{Li}({}^3\text{He}, p_5){}^9\text{Be}$ and ${}^7\text{Li}({}^3\text{He}, p_7){}^9\text{Be}$.

melting point compared with pure Li, into small islands/pieces by the volumetric expansion of liquid Li; (2) ejection of impurities on the surface of droplets, as many droplets were observed during He shot (see supplementary video S-2) and (3) dissociation of Li–O chemical bond (3.54 eV) by the impact of plasma ions and electrons. All targets were floating during exposures, thus impurity removal by He ion sputtering can be neglected.

In order to check if the removal of impurities was successful and measure the NRA spectrum of clean Li samples, both RBS and NRA were performed after the He plasma cleaning shot. Figure 4(a) shows a comparison of an RBS spectrum between an oxidized Li sample and a Li sample after He plasma cleaning. The presence of the RBS O peak was very clear before cleaning, while no O was presented after cleaning, indicating a successful removal of oxide layer. The NRA spectrum of a clean Li sample (after He plasma cleaning) can be found in figure 4(b), in which an NRA spectrum from a D plasma-exposed Li sample was also added as a comparison. The red line in figure 4(b) is a typical NRA spectrum as a result of the impact of 2.5 MeV ${}^3\text{He}^+$ on pure Li, in which ${}^6\text{Li}(p_1)$, ${}^7\text{Li}(p_{0,1,2,4})$ and ${}^7\text{Li}(d_0)$ peaks can be observed clearly. The background signal could be possibly from other nuclear reaction channels, such as ${}^7\text{Li}({}^3\text{He}, p_5){}^9\text{Be}$ and ${}^7\text{Li}({}^3\text{He}, p_7){}^9\text{Be}$. After D plasma exposure, a very large ${}^2\text{D}(p_0)$ peak can be found around the energy of 11.5–13 MeV.

It should be noted that for Li samples #4 and #6 a tiny O peak was observed in the RBS spectrum (except for the center in #4, where there is no O peak) after D plasma exposure. The total areal density of oxygen in #4 and #6 was estimated to be $1\text{--}3 \times 10^{18}$ atoms/cm² and $2\text{--}4 \times 10^{18}$ atoms/cm², respectively from these RBS measurements and the maximum depth range where oxygen is present is around 10 μm . For the other samples no oxygen signal was observed and the surfaces were assumed to be clean.

3.3.3. Deuterium plasma exposure and He/H plasma removal shot. After the He plasma cleaning shots, Li samples were subsequently exposed to D plasma at different D ion fluxes and surface temperatures. During exposure all Li targets were heated by the plasma. Subsequently the targets were retracted to the TEAC to perform NRA measurements. After that, these

Li targets were put back into the target exposure chamber again to carry out either He or H plasma exposure to remove the previously retained D. All D removal shots lasted 200 s. After the D removal shot, NRA was performed again in the TEAC to check how much D remained. The exposure conditions are given in table 1. A typical time evolution and radial temperature profile for sample #8 under D plasma exposure is shown in figures 5(a) and (b) respectively.

3.4. NRA analysis for Li samples

For each Li sample several NRA measurements have been performed on the surface at different positions (see figure 6(b)). In this case we are not interested in the D profile in the tungsten, but only in the D profile in lithium. Fortunately, the D concentrations retained in W are very low compared to those in Li. Further, also the stopping power in W is much larger than in Li. The consequence is that the contribution of D in tungsten to the D feature in the NRA spectrum can be neglected. Of course the ion fluence has to be corrected for this. Therefore, the incident fluence of ${}^3\text{He}$ on Li was deduced from the NRA spectrum by scaling the Li spectrum part (total integration of yield from energy 0.8 MeV to 10 MeV in figure 4(b)) of D-plasma-exposed Li samples with that of a pure clean Li sample. In this way, the accurate ${}^3\text{He}$ fluence bombarding Li can be obtained.

An additional complication is that, as can be seen in figure 4(b), the proton spectrum from ${}^2\text{D}(p_0)$ overlaps with the proton spectrum from ${}^6\text{Li}(p_1)$. However, due to the low cross-section of ${}^6\text{Li}(p_1)$, this small peak does not strongly affect the measured D concentration. In any case we subtract this signal by the Li signal normalization described in the above paragraph.

4. Deuterium retention results and discussion

4.1. Target surface morphology under D plasma exposure

Figure 6(a) shows IR images of all Li sample surfaces during D exposure at steady state, in which the peak surface temperature, the plasma flux in the target centre and the total D plasma exposure time were indicated for each sample; (b)

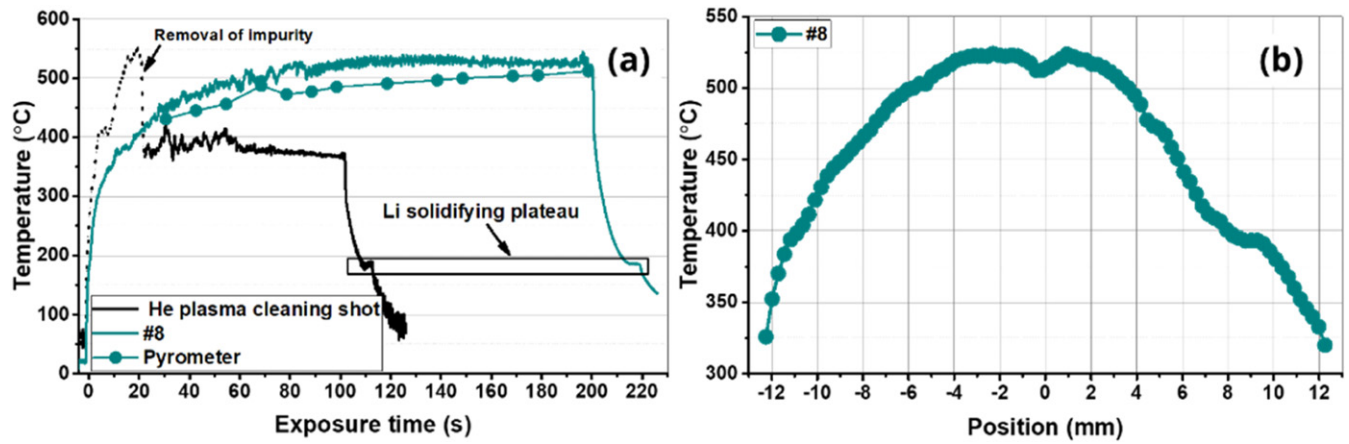


Figure 5. (a) Time-evolution of surface temperature during a He plasma cleaning shot and a D plasma exposure. Emissivity 0.1 was applied after the removal of impurity for the cleaning shot; and an emissivity 0.9 was used for Li sample #8 under D plasma. Temperature plateau during cooling-down process is marked in black square; (b) surface temperature radial profile for Li sample #8 under D plasma exposure.

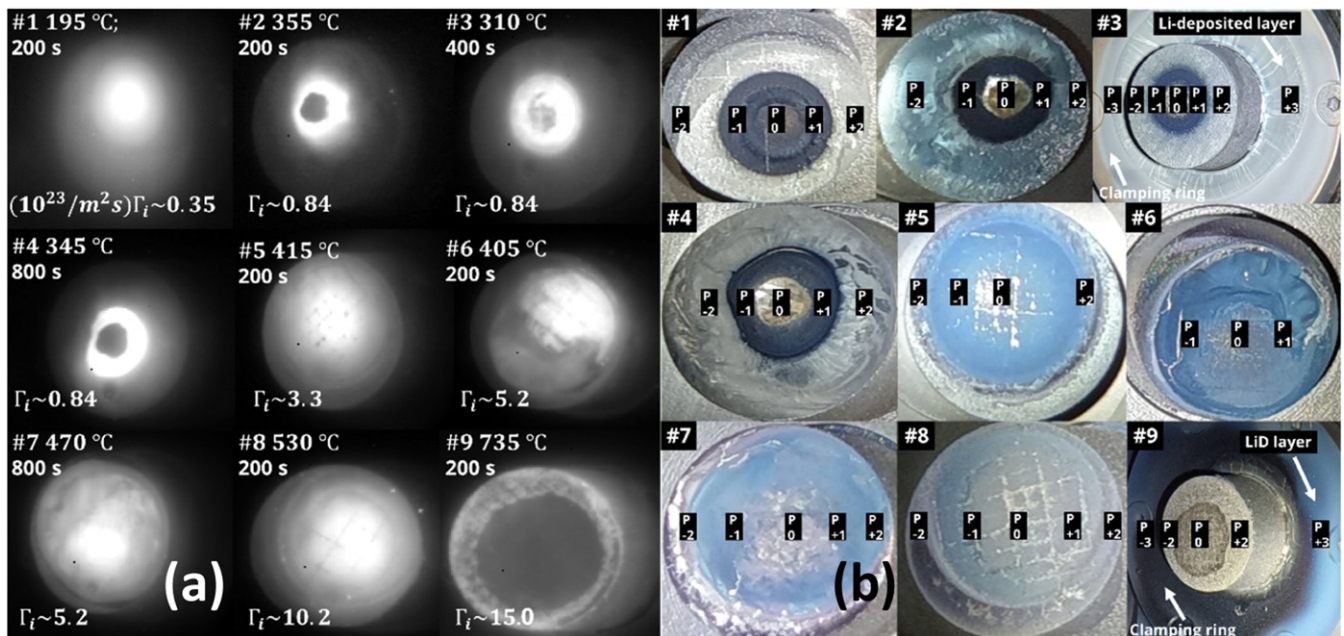


Figure 6. (a) IR images of all sample surfaces during D plasma exposure at steady state. The peak temperature and flux and the total exposure time were shown; (b) sample surface photos after D plasma exposure, taken in the TEAC without breaking vacuum. Very thick Li deposited layer was seen on the clamping ring of #3 and #9.

shows the corresponding sample surface photos after exposure, taken by a camera in the TEAC (*in vacuo*) before the post-mortem NRA measurement, in which NRA measurement positions and dimensions have been indicated for each sample. Position P_0 indicates the NRA measurement at the plasma-beam center and $P - 1$ and $P + 1$ correspond to the NRA measurements on the left and right side of the center which are around 3–4 mm away from it; $P - 2$ and $P + 2$ are also on the left and right side, respectively, which are 6–10 mm away from the center depending on the sample itself; while, $P - 3$ and $P + 3$ are the positions of NRA measurement performed on the molybdenum clamping ring on both sides. Due to the constraint of operational time, not every position mentioned above were performed on every sample.

The surface changes of Li samples under different temperatures and D ion fluxes can clearly be observed in figure 6(a). For very low flux ($0.35 \times 10^{23} \text{ m}^{-2} \text{ s}^{-1}$) at low temperature ($\leq 195 \text{ }^\circ\text{C}$), the whole surface of Li sample #1 seemed to remain in the solid state with only the temperature of the centre exceeding the Li melting point. After exposure a black circular area was presented in the centre corresponding to plasma beam width ($\sim 17 \text{ mm}$). When the D ion flux increased to $0.84 \times 10^{23} \text{ m}^{-2} \text{ s}^{-1}$, the central temperature was raised to 310–355 °C for Li samples #2, #3 and #4, which had the same exposure conditions but different exposure times. A dark liquid area (low emissivity $\varepsilon \sim 0.15$) appeared in the center for #2 and #4, encircled by a high emissivity ring ($\varepsilon \sim 0.6$). Possibly due to a slightly lower central temperature, a dark liquid area

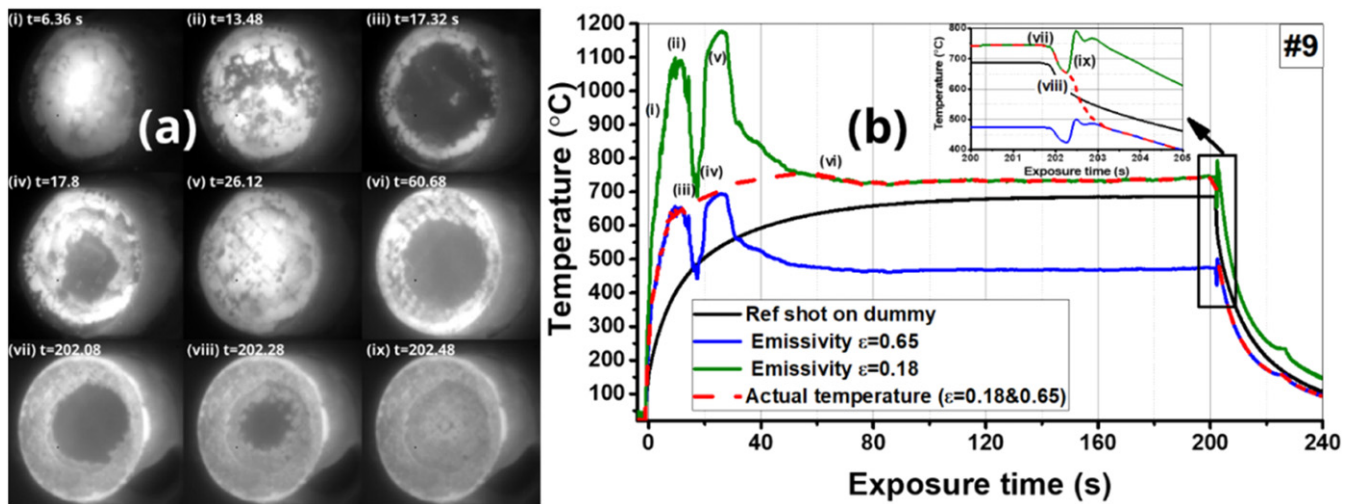


Figure 7. (a) Time-evolution of Li target #9 surface under D plasma at the flux $\sim 1.5 \times 10^{24} \text{ m}^{-2} \text{ s}^{-1}$; (b) the corresponding temperature evolution of the centre part of #9. The blue solid line is with emissivity $\varepsilon = 0.65$ for the solid state and the green solid line is with $\varepsilon = 0.18$ for liquid state, while the actual temperature is plotted by a red dash line combined with these two cases. The temperature evolution from a reference shot on the molybdenum dummy with the same condition is also presented.

was not clear in the center of #3 but was also high emissivity ($\varepsilon \sim 0.65$). In the area outside this a region of intermediate emissivity ($\varepsilon \sim 0.5$) was observed for all three targets. After exposure three corresponding regions were observed (figure 6(b)). A metallic surface, can be seen in the center of #2 and #4, while for #3 the center was duller grey. A black ring, similar to the black region for sample #1, can be observed, corresponding to the high emissivity region. Outside the black ring, the area became a blue-grey. When plasma flux was continued to increase in the range of $3.3\text{--}10.2 (\times 10^{23}) \text{ m}^{-2} \text{ s}^{-1}$ with the temperature around $405\text{--}530 \text{ }^\circ\text{C}$, the entire surfaces of Li samples #5 to #8 appeared to be in the solid state during the exposure, as seen in figure 6(a). This solid layer has a very high emissivity around $\varepsilon \sim 0.6\text{--}0.9$. A blue surface can be observed for #5 to #8 in figure 6(b) after exposure. When a higher flux ($15.0 \times 10^{23} \text{ m}^{-2} \text{ s}^{-1}$) was applied to Li sample #9, leading to a high temperature ($735 \text{ }^\circ\text{C}$) above LiD melting point ($690 \text{ }^\circ\text{C}$), a large central area liquified during exposure, and a grey metallic surface was observed again after exposure.

Two cases of strong Li evaporation were observed in the experiment. One happened on Li sample #3 during He plasma cleaning shot as mentioned in section 3.3.2, which led to a thick pure Li deposition layer on the clamping ring (see #3 in figure 6(b)). After D plasma exposure, this Li deposition layer remained a similar metallic grey color as it was before. The other case occurred on sample #9 during D plasma exposure due to the high surface temperature. This led to a thick blue layer on the clamping ring, as also can be seen in #9 in figure 6(b). No significant Li deposition layer was observed on the clamping ring for the other 7 Li samples.

As discussed in section 2.3, with the presence of colloidal lithium in LiD, the appearance of LiD crystal can be blue or coal-black, which is exactly in agreement with the appearance of Li samples displayed in figure 6(b). This indicates that LiD has formed during D plasma exposure and the observed

solid surface in figure 6(a) should be the Li–LiD colloid with different LiD fraction. It can also be deduced therefore that the blue deposited Li layer on the clamping ring of #9 is mostly LiD.

Among all Li samples, #9 was exposed to the highest D plasma flux ($1.5 \times 10^{24} \text{ m}^{-2} \text{ s}^{-1}$) and a high temperature above LiD melting point has been achieved as shown in figure 7, in which a clear phase transition was exhibited. Figure 7 shows the time evolution of the surface as observed by IR camera. During the first ~ 10 s of D plasma exposure, a solid surface (figure 7(a.i)) was quickly formed with a high emissivity ($\varepsilon \sim 0.65$) as the temperature quickly rose from room temperature to $\sim 630 \text{ }^\circ\text{C}$. At this point a liquid surface appears and the solid layer, which appears to be a thin layer on top of the liquid, breaks up (figure 7(a.ii)) until a liquid Li surface appears in the central region. This process was characterized by a sudden drop in emissivity roughly from 0.65 to 0.18, as seen in figure 7(b). Within 0.1 s after a liquid Li surface appears, the surface emissivity rapidly rises back to 0.65, indicating the formation of LiD. Around ~ 8 s later, an entirely solid surface was formed. This process was described by (iii) \rightarrow (iv) \rightarrow (v) in figure 7(a). When the temperature continued to increase and reached around $\sim 690 \text{ }^\circ\text{C}$, the solid surface slowly disappeared, which was presumably accompanied with LiD melting and its fast decomposition, until a large region in the liquid state had developed in the central area, as shown in figure 7(a.vi). This central area remained liquid for the rest of the exposure and became solid when it cooled below $690 \text{ }^\circ\text{C}$ at the end of the discharge, as shown in figures 7(a.vii)–(ix)). The clear temperature change can be seen in the inserted figure in figure 7(b). Thus, a complete process of LiD melting and solidification has been clearly observed. It should note that at the end of cooling down, a short temperature plateau (from 224 s to 227 s) close to Li melting point ($\sim 180 \text{ }^\circ\text{C}$) can be seen. This implies that even though LiD was formed, liquid Li still dominated the bulk.

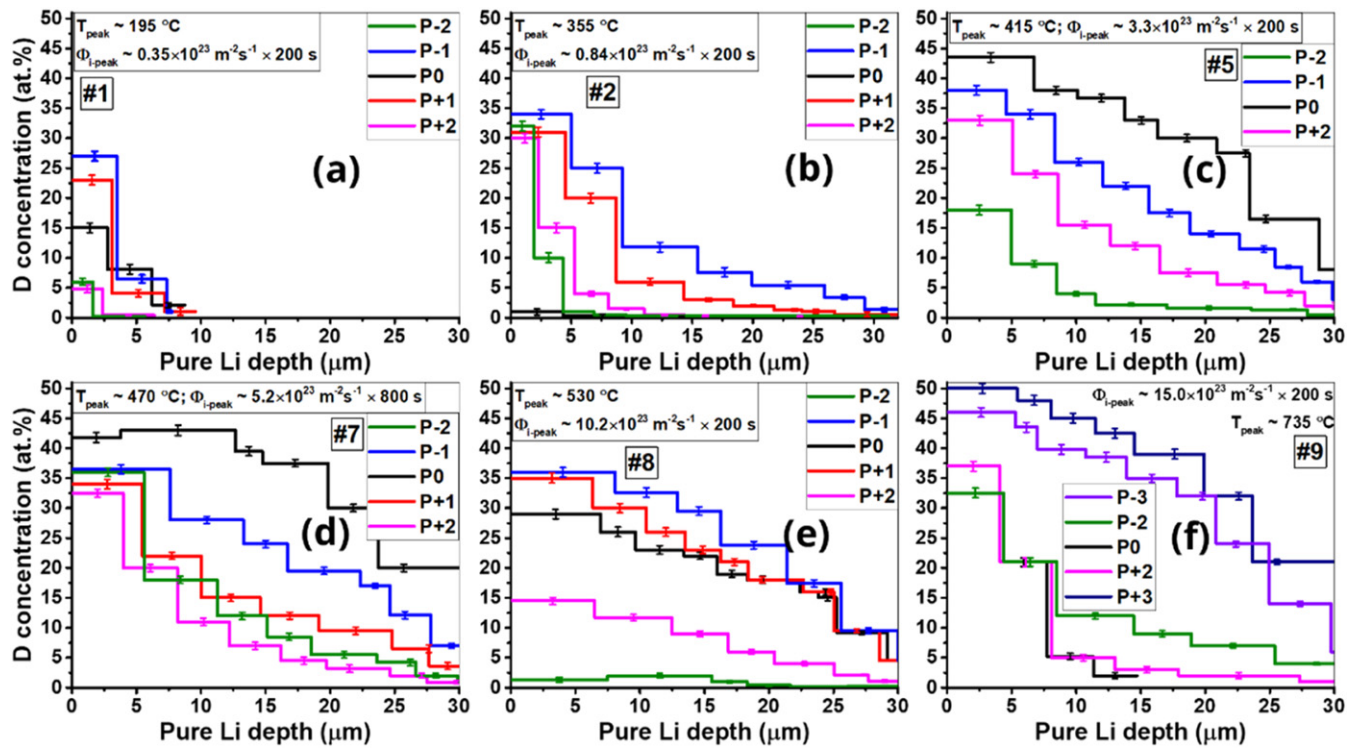


Figure 8. D concentration depth profiles at different position for Li sample #1 (a), #2 (b), #5 (c), #7 (d), #8 (e) and #9 (f). The depth is pure Li depth calculated from the number of Li atoms with the density 0.5298 g cm^{-3} . For Li, $1 \mu\text{m} = 4.60 \times 10^{22} \text{ atoms/m}^2$. The D plasma exposure time is 200 s except for (d) #7 which is 800 s.

4.2. Deuterium retention in Li after D plasma exposure

4.2.1. D concentration depth distribution. Via SIMNRA 7.02 [62] simulation, D concentration depth profiles were deduced, which are presented in figure 8. NRA spectra from some Li samples can be found in the supplementary figure S-1 in which both raw data and SIMNRA simulations are displayed. It can be clearly seen in figure 8 that the surface evolution of D concentration in Li samples is strongly influenced by the D ion flux and surface temperature. Several observations can be made from the results:

- For both low flux and low temperature D plasma exposure (figure 8(a)), D was mainly retained in the top layer ($\sim 7 \mu\text{m}$).
- As the flux and temperature increased (figures 8(b)–(d)) more D was retained and D diffused deeper. D concentration reached 30–45 at.% within the first $\sim 5 \mu\text{m}$ for these cases, and the higher flux and temperature, the more and deeper the D is retained, up to the probing depth of the NRA technique.
- As the flux continued to increase, leading to an increase in temperature (figures 8(e) and (f)), the D concentration at central position $P0$ firstly started to decrease (figure 8(e)) and was lower than that at $P \pm 1$. For very high temperatures (figure 8(f)) the D concentration in Li sample surface was found to significantly decrease. A very high D concentration was observed in the deposited Li blue layer on the clamping ring.
- The D concentration at different positions on the same sample surface varied a lot. For sample #5 and #7, the highest D concentration was found to be at the target center (position $P0$) and D concentration decreased with the distance from the center. For #1 and #8, the highest D concentration was found to be at position $P - 1$ and $P + 1$, while $P0$ showed a lower D concentration. D concentration was roughly the same for all positions on sample #9. Surprisingly, a significantly lower D concentration was observed in the center of sample #2 compared to the surrounding area, which corresponds to the shiny metallic area in figure 6(b). The same behavior was also observed for sample #4, in which the same D flux was applied and the similar temperature distribution was observed.
- Comparing all Li samples, the highest D concentration was found at several positions, namely $P0$ of #7 with 800 s exposure time, $P - 3$ and $P + 3$ on the clamping ring of #9 with 200 s exposure time, in which the D concentration was as high as 45%–50%. The D concentration at $P0$ of #5 is roughly in the similar level but with a higher gradient.

The values of the D concentration near the surface (top $\sim 1 \mu\text{m}$ layer) are plotted in the Li–LiD phase diagram in figure 1. The experimental data points are divided into four groups according to their surface appearance, namely, metal shiny, grey, black, blue. It is found that the D concentration at every position is almost beyond the solubility limit except for the metal shiny group. This suggests that D is mainly retained in the form of LiD in this experiment, which agrees with the observed appearance of Li samples after exposure in figure 6.

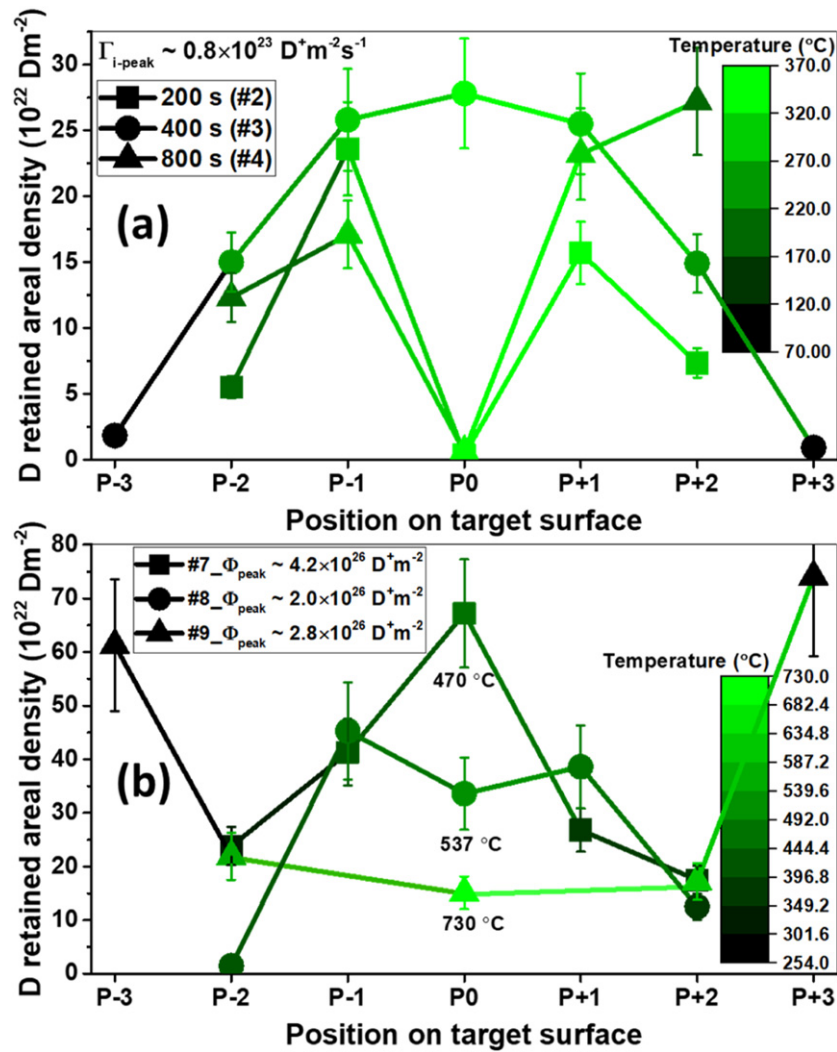


Figure 9. (a) Deuterium retained areal density in different positions of Li sample #2, #3 and #4 at $\Gamma_{i\text{-peak}} = 0.84 \times 10^{23} \text{ m}^{-2} \text{ s}^{-1}$ with exposure time at 200, 400 and 800 s, respectively. (b) Surface distribution of deuterium retained areal density at different temperature with fluence in the range $2.0\text{--}4.2 \times 10^{26} \text{ D}^+ \text{ m}^{-2}$. The fluence showed in the figure is the peak value at central position P0, while the fluence distribution over the surface is close to Gaussian. The temperature of each position is indicated by the color bar.

For the metal shiny surface (position P0 of #2 and #4), D concentration is almost aligned with the solubility, which would suggest no LiD presented. For the blue surfaces including the D-Li deposited layer, the D concentration is in the range of 17–50 at.% and the corresponding temperature is around 200–500 $^{\circ}\text{C}$, the black surfaces correspond to a D concentration of 15–35 at.% and the temperature below 320 $^{\circ}\text{C}$. While, the grey surfaces could appear at a wide temperature range from below 180.5 $^{\circ}\text{C}$ to above 690 $^{\circ}\text{C}$, corresponding to D concentration below 37 at.%.

4.2.2. Overview of total D retention within the probing depth.

The total D retained areal density (D m^{-2}) in the probing range at each position for the Li samples exposed to the same D plasma flux with different exposure time are shown in figure 9(a). The peak of the applied D ion flux is $0.84 \times 10^{23} \text{ m}^{-2} \text{ s}^{-1}$ and the exposure time was 200, 400 and 800 s, respectively. D retained areal density on the surface of the samples in figure 9(a) is in the range of $0.4\text{--}2.8 \times 10^{23} \text{ D m}^{-2}$.

As a comparison, if a pure LiD (D/Li = 1:1) layer with the same thickness as the NRA probing depth is assumed, this will give a D areal density of $9.5 \times 10^{23} \text{ D m}^{-2}$. It should be noted that possibly due to the presence of some oxygen, the sample #4 with a long exposure time of 800 s did not show higher D retained areal density compared with #2 and #3. As no significant oxygen signal was found on the surface of #2 and #3, they can be assumed to be free of oxygen. The influence of incident D plasma fluence on D retained can be clearly seen on position $P \pm 1$ and $P \pm 2$ for #2 and #3. D retained in #3 at these four positions is, averaged, 1.9 times higher than that in #2, corresponding to a factor of 2 in incident D fluence. D retained at position $P \pm 3$ of #3 on the clamping ring, where the pure Li deposition layer was pre-formed before D plasma exposure, was around $0.9\text{--}1.8 \times 10^{22} \text{ D m}^{-2}$ which was quite low as expected due to significantly low flux on the clamping ring. As shown in figure 8(b), very low deuterium concentration was found at position P0 of #2. The similar finding was also observed at P0 of #4. This low concentration reasonably

contributes to a low deuterium retained areal density at $P0$ of #2 and #4, which was around $4\text{--}6 \times 10^{21} \text{ D m}^{-2}$. Compared with $P0$ of #2 and #4, $P0$ of #3 shows a much higher D retained areal density, which could be due to a lower temperature, as discussed in section 4.1, resulting into being almost solid-state during exposure and duller grey appearance after exposure.

Figure 9(b) displays the deuterium retained areal density at different position for Li sample #7, #8 and #9, where the surface temperatures are different while with the peak fluence in the range $2.0\text{--}4.2 \times 10^{26} \text{ D}^+ \text{ m}^{-2}$. For the case of #7 exposed at relative low temperature ($T_{\text{peak}} \sim 470 \text{ }^\circ\text{C}$), the maximum deuterium retained areal density was found at the position $P0$ and was $6.7 \times 10^{23} \text{ D m}^{-2}$, which was expected as the fluence at $P0$ was the highest. However, for the case of a higher temperature exposure ($T_{\text{peak}} \sim 537 \text{ }^\circ\text{C}$ for #8), $P0$ exhibited a lower deuterium retained compared to position $P \pm 1$. From equation (2), a LiD decomposition pressure of 49 Pa (more accurately, it is in the range of 16–140 Pa if the uncertainties of temperature were taken into account) was calculated. The background neutral gas pressure is several Pa (1–5 Pa), and the neutral gas pressure close to target surface from Ray's simulation [63] is around 5 Pa, corresponding to a LiD decomposition temperature $\sim 477 \text{ }^\circ\text{C}$. In plasma environment, not only can neutral gas pressure influence LiD decomposition, but also plasma pressure could have an influence on LiD decomposition. In Magnum-PSI, compared to plasma pressure the neutral pressure close to the target is not so important. Therefore, we could attempt to apply plasma pressure to counterbalancing LiD decomposition plasma and judge if LiD could decompose. The plasma pressure can be estimated according to $P = 2n_e k T_e$, which was around 49 Pa. These suggest that the decrease of D retained at position $P0$ of #8 was possibly due to LiD decomposition. For #9, the surface temperature reached a high value of $\sim 735 \text{ }^\circ\text{C}$, which was beyond LiD melting point, and the surface in the center was also presented as liquid. The corresponding decomposition pressure is around $1.3 \times 10^4 \text{ Pa}$, and much higher than the plasma pressure (70 Pa). This indicates strong decomposition of LiD for #9, leading to a low deuterium retained areal density. However, as indicated in figure 8(f), very high D concentration was found at the Li deposition layer on the clamping ring, which corresponds to a deuterium retained areal density around $6\text{--}7 \times 10^{23} \text{ D m}^{-2}$, which is very close to the saturation value ($9.5 \times 10^{23} \text{ D m}^{-2}$).

Figure 10 displays an overview of D retained fraction in all Li samples as a function of temperature. The fluence for each point is indicated by the color bar. The data points can be roughly divided/classified into two groups. One group was exposed at low flux ($< 10^{23} \text{ m}^{-2} \text{ s}^{-1}$) and the another one was with higher flux ($> 10^{23} \text{ m}^{-2} \text{ s}^{-1}$). For the low flux group, the corresponding fluence is also relatively low ($< 10^{26} \text{ m}^{-2}$) and the temperature is in the range of 100–350 $^\circ\text{C}$. The deuterium retained fraction slowly increases with temperature and varies from 0.1% to 2%, and suddenly drop to significantly low value around 0.001%–0.03%. For the case of high flux group, the corresponding achieved temperature is above 300 $^\circ\text{C}$. It can be seen that the D retained fraction also slowly increases with temperature until 500 $^\circ\text{C}$, and then decreases.

According to above results and discussion as well as target surface morphology in section 4.1, the entire process of D plasma interacting with clean Li targets can be described as below:

- (a) Formation of solid Li–LiD layer below $\sim 180.5 \text{ }^\circ\text{C}$. When Li target was heated from room temperature to Li melting point by D plasma, a thin solid Li–LiD layer could be formed on the surface. The presence of LiD significantly lowered deuterium surface recombination and the surface turned to be completely recombination-limited. This resulted into a high D retained concentration in the very top layer, which is the case of target #1.
- (b) Breaking down of Li–LiD layer due to volumetric expansion of liquid Li coming from inside above 180.5 $^\circ\text{C}$. As the temperature continues to increase from Li melting point to a higher value, pure liquid Li could volumetrically expand and come from inside bulk, leading to breaking down of the Li–LiD layer. The coming fresh liquid Li is characterized by a high deuterium surface recombination coefficient, making it close to diffusion-limited regime. In this case, if the applied ion flux is low, which was around $\sim 8 \times 10^{22} \text{ D m}^{-2}$ in this experiment, the D surface recombination flux to the vacuum can be so high that the implanted D concentration is limited below its solubility limit, and the surface will remain in the liquid state with dilute D solution. This has been observed on the surface of #2 and #4, which is exactly in the agreement with our hypothesis in section 2.2. But if the applied ion flux is high enough, once liquid Li is presented the implanted D concentration can be immediately beyond its solubility limit, leading to solid LiD formation. Then the surface returns to recombination-limited recycling with very low surface recombination coefficient. This phenomenon also occurred during the time evolution of the surface of #9 as discussed in section 4.1 (figure 7).
- (c) The Li–LiD layer formed in (a) will not be broken down if it is too thick or there is just no fresh pure liquid Li presented. In this case, the Li–LiD layer can grow thicker and will be presented as a colloid resulting into a high D concentration. This is the case for Li target #5 to #8.
- (d) Competition of LiD formation and decomposition. In figure 9(b) D retention was found to decrease when LiD decomposition pressure can be comparable to plasma pressure. This could imply that the decrease is due to decomposition of LiD. As LiD decomposition pressure grows exponentially with temperature, LiD decomposition would dominate the D retention process when temperature is high, and lower D concentration. This domination starts to occur at temperature around 500–550 $^\circ\text{C}$ in our experiment.
- (e) Melting of LiD. When target temperature continues to increase beyond the melting point of LiD, the Li–LiD colloid would melt mostly possibly accompanied with strong LiD decomposition, and the surface will turn back to liquid, as seen in figure 7.
- (f) Co-deposition of Li and D in form of LiD. If the surface is presented as liquid at high temperature, for example

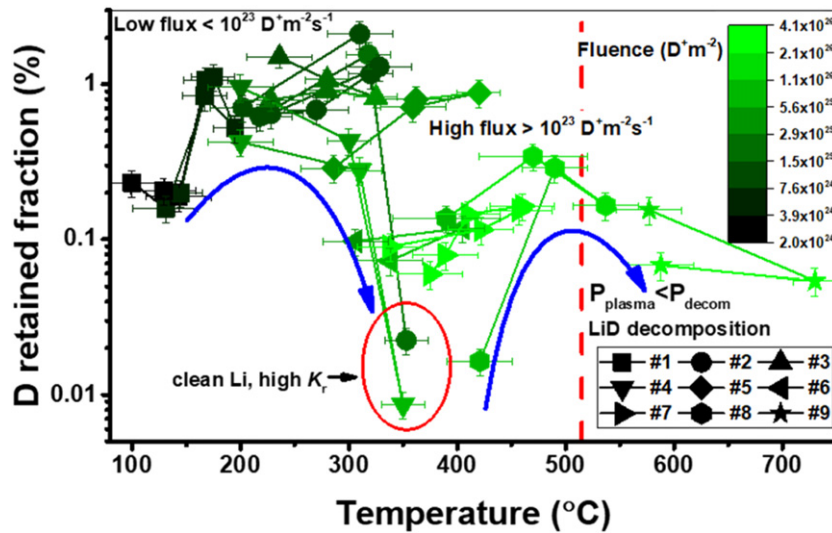


Figure 10. Deuterium retained fraction in NRA depth probing as a function of temperature for all Li samples exposed at different fluence. The fluence for each point are indicated by the color bar. The blue arrows are added to guide the eye to show the trend of the fraction as temperature increases. Clean fresh liquid Li with high surface recombination coefficient K_r was presented for the data points in the red circle region. The red dashed line indicates the region where the decomposition pressure of LiD is beyond the plasma pressure.

LiD melting in (e), strong Li evaporation becomes possible. This would lead to strong co-deposition of Li with D on cold surrounding areas. The deposited layer seems to be pre-dominantly LiD in this experiment. LiD itself will not strongly evaporate at this temperature and would in any case quickly dissociate in the plasma. Therefore, the thick LiD region on the clamping ring of #9 in this experiment was most likely formed by the co-deposition of evaporated Li atoms with D atoms.

It should be noted that in process (b), high D diffusivity, convection and turbulence for the fresh liquid Li in the center should be also taken into account. On the one hand, convection can bring these D atoms dissolved in top Li layer to deep layer before they form LiD. On the other hand, turbulence can also help outgas these dissolved D atoms and let them escape from Li and lower D concentration. What's more, high D diffusivity in pure liquid Li can also enhance D diffusing either out of the surface or forward deeper.

4.2.3. Comparison between experimental data and 1D RD model.

4.2.3.1. Estimation of reaction rate constant As a solid surface has been found to quickly present on many Li surfaces under D plasma exposure in the experiments, thus it is reasonable to assume a very 'thin' LiD layer on the very top surface of Li samples under D plasma and apply deuterium diffusivity in LiD to equation (7) to estimate the implanted deuterium atom concentration.

From equation (6) and using initial condition $n_{Li}(t=0) = n_0 \approx 4.5 \times 10^{28} \text{ m}^{-3}$, the change of Li atom concentration can be expressed as

$$n_{Li} = n_0 e^{-kn_D \cdot t} \quad (10)$$

which can be rewritten as

$$k = -\frac{\ln\left(\frac{n_{Li}}{n_0}\right)}{n_D \cdot t}, \quad (11)$$

where $\frac{n_{Li}}{n_0} = \frac{n_0 - n_{LiD}}{n_0}$ can be deduced from the retained D concentration in top several micrometers measured by NRA (figure 8), assuming all D exists in the form of LiD after deuterium plasma exposure; t is plasma exposure time (reaction time) in second.

Thus, from equation (11) the reaction rate constant k can be estimated. $k \text{ (m}^3 \text{ s}^{-1}\text{)} = Ae^{-E_a/RT}$ can be rewritten as the equation (12) below. $-\frac{E_a}{R}$ is the slope of the linear plot by $\ln k$ vs $\frac{1}{T}$. Figure 11 displays the fitted activation energy from #5 and #7, in which the decomposition of LiD can be ignored and no obvious macroscopic surface motion was observed during the exposure.

$$\ln k = \ln A - \frac{E_a}{R} \cdot \frac{1}{T} \quad (12)$$

Taking the average value of activation from #5 and #7, thus an experimental expression for reaction rate constant can be expressed as

$$k \text{ (m}^3 \text{ s}^{-1}\text{)} \approx 10^{-(25 \sim 26)} \cdot e^{-(3 \pm 1) \times 10^4 / RT}. \quad (13)$$

Equation (13) indicates that the reaction rate constant increases with increasing temperature, resulting into a fast reaction rate of Li with deuterium atoms, thus a higher deuterium retained. This is also in agreement with our observation in figure 10 if LiD decomposition is ignored. It should be noted that equation (13) is an estimation from the experiment assuming a bulk of D atoms are interacting with a bulk of fixed Li atoms. The estimation can be influenced by the applied D diffusivity and the estimation of D concentration due to plasma implantation.

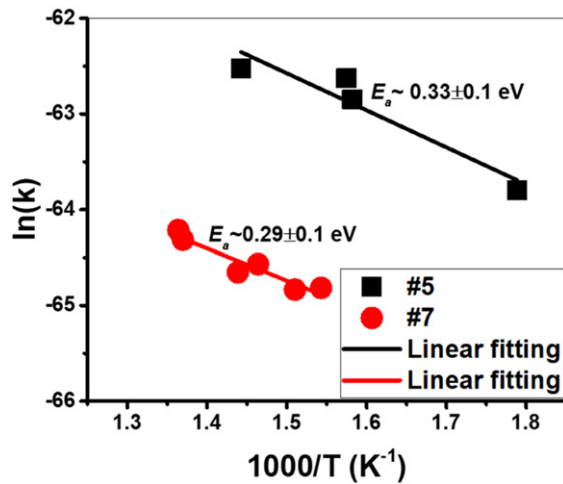


Figure 11. Rate constant (in the form of $\ln k$) as a function of temperature (in the form of $\frac{1000}{T}$).

4.2.3.2. D depth profiles from 1D RD model To make a fair comparison with NRA measurement, Li target #5 was chosen to model as for #5 there was (1) no phase transition, (2) no LiD decomposition; and (3) LiD was not saturated during the whole exposure time; and (4) the surface is roughly uniform. Figure 12 shows a comparison between the modelling result from RD model and NRA measurement for Li target #5. The bold solid lines are the D depth profiles from NRA and the dashed lines are the RD modelling results using deuterium diffusivity as a function of LiD concentration. It can be seen that the modelling results are a little higher than NRA results. Two possible reasons are involved. One is that in the RD model, the radial diffusion of D atoms and the convection are not considered, and Li/LiD diffusion and temperature gradient are also neglected. Another one is that these diffusivities from MD simulation [47] may not perfectly match the actual diffusivity in experiments. To gain an optimized/better modelling result of D depth profiles, an effective diffusivity D' as a constant was introduced by matching the modelling deuterium depth profiles to the NRA depth profiles. The optimized modelling of D depth profiles is displayed by thin solid lines in figure 12.

By using the same initial and boundary conditions as that of position P_0 of #5 in figure 12, a prediction for deuterium retained concentration depth profiles in 1 mm thick Li target at different exposure time is displayed in figure 13, in which $D = D(f)$ was applied to (a) and $D = D' = 4 \times 10^{-9} \text{ m}^2 \text{ s}^{-1}$, which was determined from P_0 of the sample #5, to (b). It can be seen that for both cases deuterium is mainly retained in top $\sim 100 \mu\text{m}$. For the case of (a), a thick Li layer with a deuterium concentration of 50 at.% seems difficult to achieve due to the decrease in D diffusivity as the LiD concentration increases. For (b), even though a constant diffusivity is assumed throughout the whole depth, the growth of Li layer with high D concentration ($\sim 50 \text{ at.}\%$) is getting slower and slower, which is expected as it would take more time for D atoms to diffuse deeper, thus limiting the production rate of LiD. In principle, given enough time an almost pure LiD layer ($D\% \sim 50 \text{ at.}\%$) could be possible but its thickness is effectively limited to the

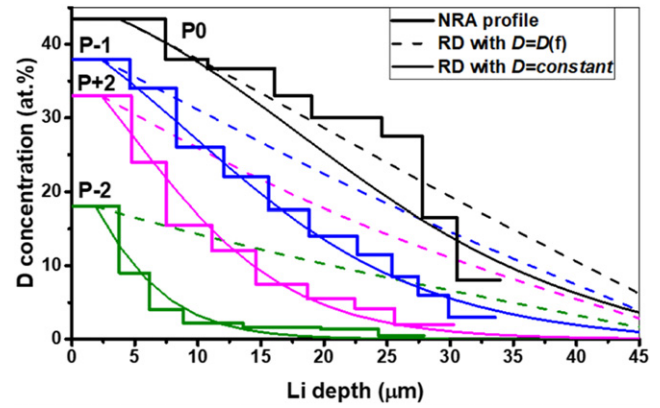


Figure 12. A comparison of deuterium depth profiles between NRA and RD model with $D = D(f)$ and $D' = \text{constant}$ (effective diffusivity), respectively. The effective diffusivity D' is 1.4×10^{-10} , 2.1×10^{-9} , 4×10^{-9} and $1.2 \times 10^{-9} \text{ m}^2 \text{ s}^{-1}$ for $P - 2$, $P - 1$, P_0 and $P + 2$, respectively. (The reason that #5 was chosen to study the RD model and make the comparison with NRA is that for #5, (1) no phase transition; (2) no LiD decomposition; (3) LiD was not saturated during the whole exposure time; (4) the surface is roughly uniform).

top 10–100 μm layer. An indication that this is the case in the experiment can be found at position P_0 of Li sample #7 in figure 8, where D concentration approaches 50% but only over the first $\sim 20 \mu\text{m}$. Figure 13(c) exhibits total D retained areal density and D retained fraction in 1 mm thick Li extracted from (a) and (b) as a function of time. When $D(f)$ was applied the D retained areal density increases with the fluence roughly as a scaling of $\Phi^{0.5}$ and gets slowly after 400 s, and a ‘saturation’ value could be predicted around $1.6 \times 10^{24} \text{ D m}^{-2}$. However, for the case of D' , a ‘saturation’ value for D retained areal density cannot be assumed as the diffusivity is not affected by LiD concentration. However, in such a case the effective diffusivity assumption is probably questionable. Also, a rate of increase goes as $\Phi^{0.7}$. However, both cases suggest a low D retained fraction around 1.2%–2.3% in the beginning and then decreasing with increasing time (fluence). This is in agreement with our experimental observation in figure 10.

5. Deuterium removal

The above observations have indicated that deuterium retained in Li still can be much higher compared to that retained in tin and tungsten [30]. Such high concentration in Li has to be removed in the case of tritium to avoid safety concern and recycle precious tritium. In order to understand how well these deuterium atoms retained in Li can be removed by plasma exposure, both helium and hydrogen plasmas were applied to D-plasma-exposed Li samples to remove the retained D. The applied conditions of He and H plasma exposure were also listed in table 1.

5.1. Helium plasma

He plasma has been utilized to remove the retained deuterium in targets #2, #5 and #9. The result is shown in figure 14, in which the remained D in forms of both the absolute areal

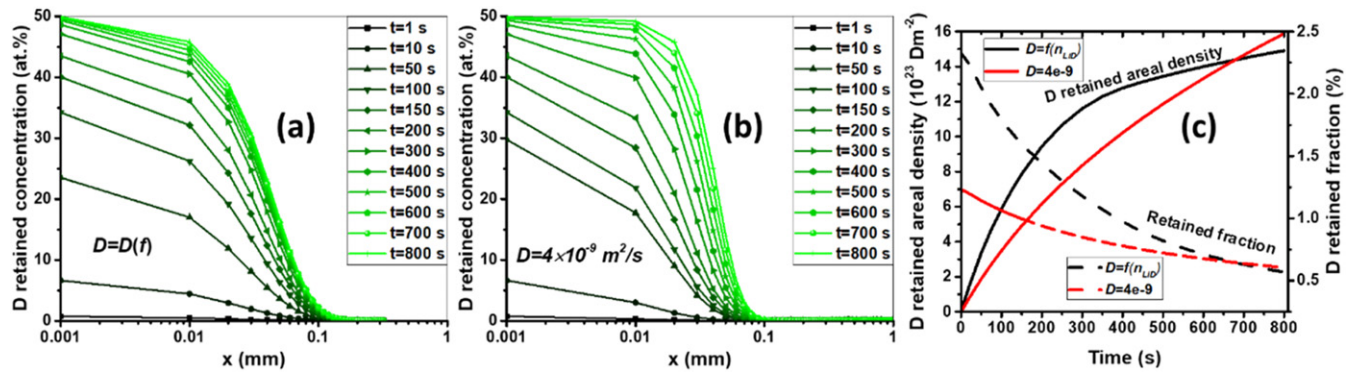


Figure 13. D concentration depth profiles at different time with (a) $D = D(f)$ and (b) $D = D' = 4 \times 10^{-9} \text{ m}^2 \text{ s}^{-1}$ (c) deuterium retained areal density and retained fraction in 1 mm thick Li as a function of time from RD model ($\Gamma_i = 3.3 \times 10^{23} \text{ m}^{-2} \text{ s}^{-1}$).

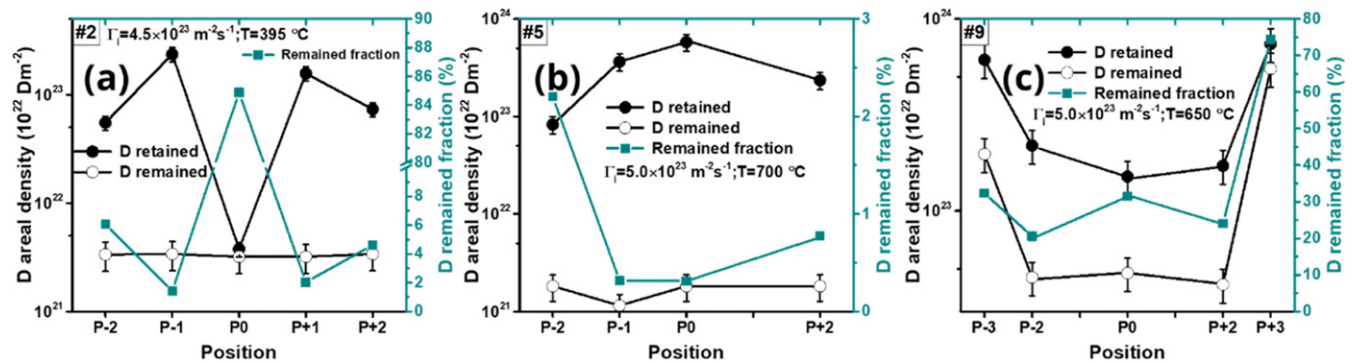


Figure 14. D remained areal density and fraction after He plasma on D-plasma-exposed Li target. (a) Li target #2 with $T \sim 400 \text{ }^\circ\text{C}$; He ion flux $\sim 4.5 \times 10^{23} \text{ m}^{-2} \text{ s}^{-1}$; (b) Li target #5 with $T \sim 700 \text{ }^\circ\text{C}$; He ion flux $\sim 5.0 \times 10^{23} \text{ m}^{-2} \text{ s}^{-1}$; (c) Li target #9 with $T \sim 650 \text{ }^\circ\text{C}$; He ion flux $\sim 5.0 \times 10^{23} \text{ m}^{-2} \text{ s}^{-1}$.

density and the remained fraction ($D_{\text{remained}}/D_{\text{retained}}$) after He plasma removal is plotted at different position over the surface. The original D retained after D plasma exposure is also added as a comparison. The remained D concentration depth profiles are displayed in supplementary figure S-2. Figure 14 clearly indicates that after He plasma the remained D in the surface has significantly decreased. For #2, a nearly uniform D remained areal density around $3 \times 10^{21} \text{ D m}^{-2}$ was presented all over the surface and only several percentages of the retained D were left except for position P_0 where the retained D was already quite low as previously presented. #5 has exhibited a high D retained after D plasma exposure (for example, $5.8 \times 10^{23} \text{ D m}^{-2}$ at P_0), while an extremely low remained D areal density below $2 \times 10^{21} \text{ D m}^{-2}$ was found after He plasma exposure, corresponding to a remained fraction 0.3%–2.2%. As previously stated, #9 has been exposed to a very high D ion flux, leading to a high surface temperature above LiD melting point with the surface in the liquid state. The removal of D retained in #9 was also performed at a high temperature. While compared to the results from #2 and #5, the D removal result of #9 show a much higher D remained areal density on the target surface around $4.5 \times 10^{22} \text{ D m}^{-2}$, corresponding to a fraction of 20%–30%. It should be noted that after He plasma removal shot, position $P \pm 3$ on the clamping ring still exhibits a high D areal density with a fraction of 32% and 74%, indicating D

removal from Li-D co-deposition layer was not effective most likely due to low temperature and low He ion flux.

The clues for the explanation to the above behaviors can be hinted from target surface and temperature evolutions and also the remained D depth profiles. The time evolution of surface temperature during He plasma exposure can be found in supplementary figure S-3 and the IR images of #2, #5 and #9 during the exposure and the corresponding sample pictures after exposure can be found in supplementary figure S-4.

In the beginning of the He plasma, the solid colloid layer from #2 and #5 formed during D plasma exposure were broken apart by the liquid lithium expanding from inside, which was clearly seen in the IR camera video and implied by a sudden drop in emissivity drop as shown in supplementary figure S-3. In this case, liquid lithium with low D concentration can be presented on the surface, while for this solid colloid layer with high D concentration, LiD could decompose, sink or be dissolved in the liquid lithium, or just be ejected out being attached to droplets by He plasma. NRA measurement shows that the remained D concentration in top lithium is 0.2–0.8 at.% for #2 and below 0.15 at.% for #5. In the surface of #9, D concentration at P_0 , $P + 2$ and $P - 2$ was found around 5.5–7.5 at.% in top $\sim 6 \mu\text{m}$ layer and 1–3 at.% in the depth of 7–25 μm . D concentrations in the surface of these 3 targets are all on or below the level of D solubility limit, suggesting no existence of LiD after He plasma. It is also indicated

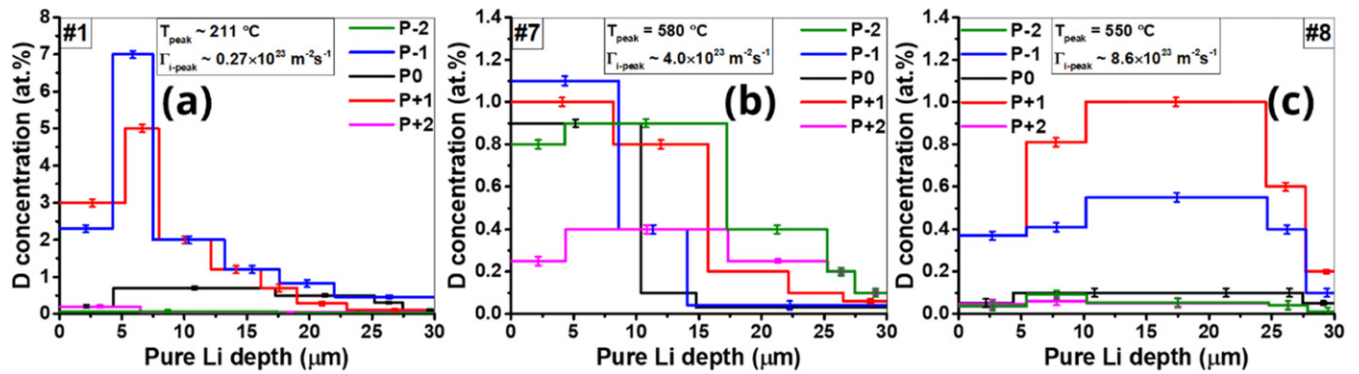


Figure 15. The remained D depth profiles for Li target (a) #1, (b) #7 and (c) #8 after H plasma exposure. It should be noted from supplementary figure S-5(a) that the whole surface of #1 and #8 is solid and the central area of #7 including position $P0$ and $P \pm 1$ is liquid, while $P \pm 2$ of #7 close to edge remained solid.

that the remained D concentration in Li-deposited layer on the clamping ring has decreased from previous 47–50 at.% to now 4–19 at.%, however, D concentration in deep layer almost did not change. This could be attributed to by either LiD dissociation or newly formed fresh Li-deposited layer.

5.2. Hydrogen plasma

After D plasma exposure, 6 Li targets were exposed to H plasma to remove the retained D. The applied H plasma conditions for each target can be seen in table 1. The IR images of these 6 targets during H plasma exposure and the corresponding target photos after exposure can be found in supplementary figure S-5. Figure 15 displays the remained D depth profiles for target #1, #7 and #8. As can be seen in supplementary figure S-5(a), the whole surface of #1 and #8 is solid and the central area of #7 including position $P0$ and $P \pm 1$ is liquid, while $P \pm 2$ of #7 close to the edge remain solid. For those positions remained solid, the maximum D concentration was not presented in top layer but in deeper layer, as seen in figure 15. Over the whole NRA probing depth, the remained D concentration first increases with the depth and then decreases with the depth, indicating that D retained in top Li layer is easier to remove as expected. On the other hand, for those positions remained liquid state during H plasma, the remained D concentration still decrease with the depth and the maximum D concentration was still in the top layer. Compared to D concentration after D plasma, the D concentration after H plasma has significantly decreases from 15–45 at.% (see figure 8) to 0.1–7 at.%. Additionally, it is also possible for the retained D to diffuse deeper during H plasma. This can be implied by a comparison in D depth profiles of #1 after D plasma and after H plasma. D was mainly retained in top 10 μm layer for the former (see figure 8(a)), while a D concentration around 0.2–2 at.% has been found in the layer of 10–30 μm for the latter.

Figure 16 shows the result of D removal by H plasma from the 6 Li samples, where the original D retained after D plasma exposure is also added. For the low temperature case of (a) #1, where the peak temperature was just above Li melting point, a high remained D areal density around $0.7\text{--}2.7 \times 10^{22} \text{ D m}^{-2}$ was found in the area including $P0$ and $P \pm 1$ with a remained fraction of 18%–43%, implying a low removing efficiency.

For sample #4, position $P \pm 2$ on the edge, where the H ion fluxes and temperatures were low, shows a high remained D areal density around $8\text{--}9 \times 10^{22} \text{ D m}^{-2}$ with a high remained fraction (30%–70%). As previously discussed, D remained in position $P0$ of #4 is extremely low, which is close to D solubility limit. However, after H plasma the D areal density almost increased by a factor 2. Several possible reasons could be attributed to this. One is that NRA measurement after H plasma was not exactly performed on the same position after D plasma and H plasma. Another reason is that the retained D could diffuse from high concentration to low concentration regions during H plasma exposure. As $P0$ was in the liquid state, the surface convection could also lead to a re-distribution of D concentration. Compared to other 5 samples, #4 displayed a relatively high remained D areal density, especially on the edge area. This could be due to that more D has diffused deeper in #4 for it was exposed to D plasma for 800 s. For these high temperature (425–600 °C) cases, such as (c) #3, (d) #6, (e) #7 and (f) #8, the remained D areal density over the whole sample surface was below 10^{22} D m^{-2} with the remained fraction below 6%.

The behaviors of Li targets exposed to H plasma are quite similar to that in D plasma. For Li samples #1, #8, #6 and #4, H exposure fluxes were slightly lower while the surface temperature slightly higher than that of D plasma exposure. While, a similar surface behavior of the targets was still presented and no melting of solid layer was observed except for the center part of #4, which is the same as that of #4 under D plasma. With no pure liquid coming from inside the LiD layer formed during D plasma, the removal of D retained can be only due to LiD decomposition/dissociation, isotope exchange or thermal desorption for high temperature cases. The post-exposure photos after H plasma (see supplementary figure S-5(a)) were not as blue or black as that after D plasma (see figure 6), possibly indicating less LiD/LiH presence, or a different color behavior of Li–LiD and Li–LiH. In [64] Christenson *et al* applied thermal treatment method to extract HIs from both Li-rich and LiH-rich samples with the design of a distillation column and their results show that the desorption peak for the former is around 400 °C and 630 °C while for the latter is around 630 °C. Compared with thermal treatment on D/T-plasma-exposed

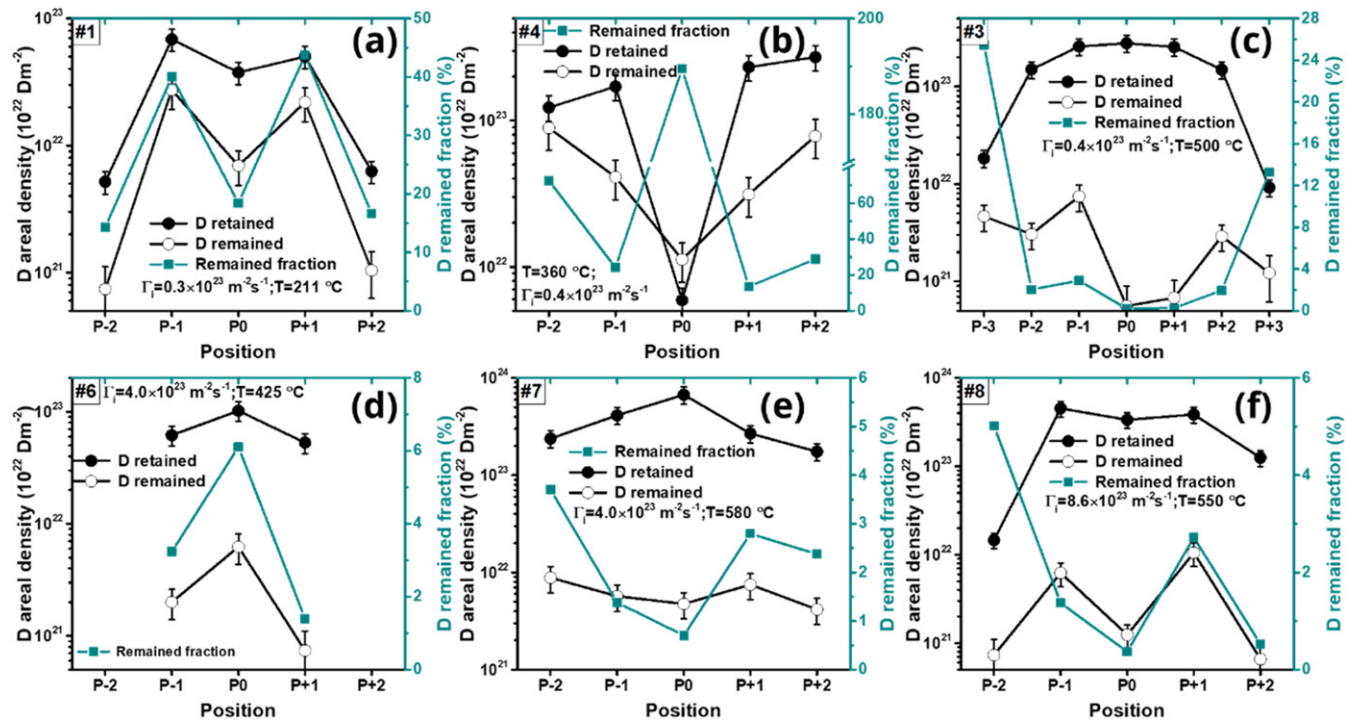


Figure 16. D retained areal density and fraction after H plasma on 6 D-plasma-exposed Li samples. Sample ID and the applied H ion flux (peak value) and surface temperature (peak value) are added to each sub-figure.

Li targets, He/H plasma treatment could be more efficient and easier to perform.

Li sample #3 under H plasma with the 2 times lower flux compared to that in D plasma exhibited a similar surface behavior in the beginning of exposure, however, as the temperature increased up to $500 \text{ }^\circ\text{C}$, the liquid area in the center started to spread out presumably accompanying with the decomposition of LiD and a shiny metallic surface was presented after exposure meaning very low H/D concentration, which is quite different from D plasma exposure where the surface temperature was around $310 \text{ }^\circ\text{C}$. This again implies that D or H retention in lithium surface can be significantly influenced by surface temperature and ion flux.

6. Comparison with literature and Implications for liquid lithium divertor

In D retention measurement in Li in PISCES-B by Baldwin *et al* using thermal desorption spectroscopy (TDS) [32], they reported a full uptake of D ions and atoms coming from plasma until the Li sample was volumetrically converted to Li deuteride (LiD), which implied that once the samples was saturated by D plasma the sample became a total LiD bulk sample with D atomic concentration at 50 at.% throughout the entire sample. However, in contrast, in our experiment we did not observe a very thick pure LiD layer except for the Li-D co-deposited layer formed during exposure at high peak temperature. The only indication of D-saturated Li was implied in the center (P0) of #7, in which a Li layer in top $\sim 12 \mu\text{m}$ with a roughly uniform D concentration at $\sim 45 \text{ at.}\%$ was found. By

using the RD model, the D retained concentration as a function of depth in 1 mm thick Li at different times can be seen in figure 13. It can be seen that D is mainly retained in top $\sim 100 \mu\text{m}$ and the trapping efficiency through 1 mm bulk Li is below $\sim 2\%$.

In [32] it is also found that the retention as measured by TDS is systematically larger than the ion fluence, while Baldwin attributed this to the neutral atom flux. We carried out a trial to measure D retained in the whole Li sample using TDS after deuterium exposure, we found that the TDS vessel was coated by a thin Li deposition layer and after the Li sample was removed from TDS setup, there was still a lot of deuterium desorption from the vessel (see supplementary figure S-6), implying that during the desorbing process of Li samples in TDS, the Li coating layer could absorb a lot of deuterium. The deuterium gas re-desorbed from the Li-coated vessel could play a role in the TDS measurement and make the total D retained in Li strongly overestimated. We cannot comment on whether this was a significant factor in [32]. However, during the transit of Li samples from plasma exposure position to TDS setup it is inevitable for the Li surface to be exposed in the air. TDS desorption profile in [32] already indicated this. We also did NRA measurement on air-exposed Li samples after D plasma exposure and found D retained in top surface has significantly decrease (see supplementary figure S-7) due to the interacting of LiD with water vapor ($\text{LiD} + \text{H}_2\text{O} \rightarrow \text{HD}\uparrow + \text{LiOH}$). If no D was absorbed by TDS vessel for the case of [32], then the total D measured in [32] should be lower than what expected. However, it is still hard to say if the escaped deuterium plays a role in the determination of D retained in Baldwin's Li samples. Another explanation for the

discrepancy between Baldwin's experiment and ours is that the Li samples they utilized were free surface, where the convection could be stronger than that in our CPS Li samples, making the mixing of deuterium with Li atoms more efficient [51]. Additionally, they applied deuterium plasma to perform Li surface cleaning and the targets were biased negatively at -50 V during the D retention shots. In our experiment Li surface cleaning was performed with helium plasma and the targets were floating during D plasma shots and measured with NRA after exposure. To conclude above discussion, the discrepancy could be mainly due to that they overestimated the total D retained while it was underestimated in this work.

In our experiment, the formation of LiD has been directly observed and D retained in the form of LiD is still proposed to be responsible for high D inventory in Li. The results suggest that D inventory related to LiD formation increases with temperature until ~ 500 °C, beyond which LiD decomposition could start to play a role. D retained concentration is the highest in top several μm , and then decreases with the depth. To achieve a limited HI inventory or a low retained fraction in liquid lithium divertor (LLD), a high temperature above ~ 500 °C could be required to dissociate LiD/LiT. However, at temperatures higher than Li hydride melting point, HI atoms would combine with evaporated Li atoms and lead to quite high HI inventory in Li re-deposited layer. The formation of the solid Li–LiD colloid, on the one hand, can stop further HI diffusion and lower HI inventory; on the other hand, it could suppress Li evaporation and Li flowing, which is not good for the heat exhaust in the divertor region and liquid refreshing and self-healing. In terms of low recycling, a low recycling regime could be achieved in the beginning, while with top Li layer becoming more concentrated in LiD, the low recycling could slowly vanish. The combination of Li vapor with HI atoms could also achieve a low recycling. While, this experiment was based on the application of static Li-filled 3D-printed W Li targets, it still remains unknown if the same behaviors will be observed for flowing Li cases. It would be recommended to investigate this question further.

Our findings also suggest that a low HI inventory could be presumed if a very fresh clean liquid Li can be obtained, in which very fast surface recombination and diffusion can pose a low HI concentration below its solubility limit to inhibit Li hydride formation. However, this cannot apply to very high flux cases as high fluxes could lead to a high implanted deuterium concentration beyond its solubility limit, subsequently to LiD formation. A possible optional operation for a LLD is to pre-expose LLD to H or D plasma to 'saturate' top Li layer and get an acceptable low HI retained fraction before performing D–T fusion plasma shot. Once tritium inventory in LLD reaches the limited value, LLD then can be exposed to D/H or He plasma to desorb T retained, as was shown in section 5. In this case, it is still needed to consider if the good evaporation and expected recycling behavior can be presumed however.

In this experiment, either solid surface (Li–LiD colloids) or liquid surface was presented, depending on both surface temperature and hydrogen plasma flux. This is summarized in

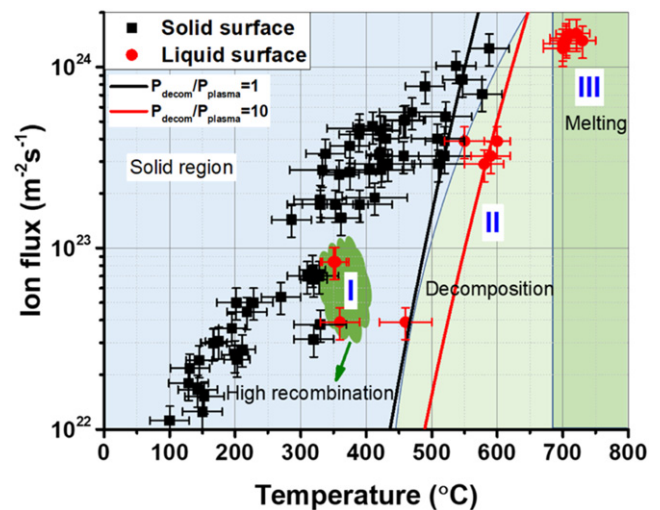


Figure 17. Surface morphology of Li samples as a function of hydrogen (D and H) ion flux and surface temperature. Three regions where the Li surface can be presented as liquid state are indicated: region I—due to high surface recombination rate; region II—due to strong decomposition; region III—due to LiD/LiH melting. All samples were floating, resulting into a ~ 5 eV ion energy. The solid black line represents the plot of $P_{\text{decom}} = P_{\text{plasma}}$, and the solid red line is the plot where the decomposition pressure of LiD is 10 times higher than plasma pressure.

figure 17. The solid surface, which is characterized with a high emissivity around 0.6–0.9, possesses a high hydrogen retention and is expected to have a low lithium evaporation. On the other hand, the liquid surface characterized by a relatively low emissivity around 0.1–0.3 displays a low hydrogen retention and possibly also a relatively high Li evaporation, though this was not directly measured, and Li evaporation from Li–LiD colloids is still remained unexplored. The liquid surface can be resulted from three mechanisms. The first one, as discussed in section 4.2.2, is the high surface recombination of hydrogen atoms on clean Li surface. This can normally be observed at a low plasma flux but where the surface temperature is relatively high, shown in region I in figure 17, where the retained D is extremely low and close to the solubility limit. High decomposition rate of Li hydride that is far beyond its formation rate is proposed to be the second mechanism. The liquid resulted from this has a higher emissivity around 0.2–0.3 compared with the liquid in region I and also a higher hydrogen retention. This case can occur at a higher flux but require a higher temperature, shown in region II. In this case, the border of liquid and solid states seems to be located between the line of $P_{\text{decom}}/P_{\text{plasma}} = 1$ and the line of $P_{\text{decom}}/P_{\text{plasma}} = 10$. The third mechanism is the melting of Li hydride once temperature is beyond its melting point, as shown in region III. The data listed in figure 17 is from the Li samples that were floated during exposure with typical ion energy around 5 eV based on Sheath theory. While, the influence of ion energy on the Li surface morphology is unclear and need to be further explored. We could possibly expect that high energy ions could lead to a decrease in temperature operation window that requires a liquid surface as these high energy ions could dissociate/break the chemical bond between Li atoms and hydrogen atoms.

7. Conclusions

The application of novel design of 3D-printed tungsten [58] provides a stable liquid lithium surface and makes it possible to expose Li to high deuterium ion flux plasma on Magnum-PSI at high temperatures. The in-house built ion-beam facility setup on Magnum-PSI makes it possible to characterize D retention in Li with an *in situ* NRA method without breaking vacuum. Taking advantage of this, Li-based 3D-printed tungsten samples were exposed to D plasma with the flux in the range of 0.4×10^{23} to $1.5 \times 10^{24} \text{ m}^{-2} \text{ s}^{-1}$, corresponding to a temperature range from below Li melting point (180.5 °C) to above LiD melting point (~ 690 °C). A solid Li–LiD colloid layer can quickly form in the beginning of exposure and its melting was found to occur at temperatures close to LiD melting point. The formation of LiD can be clearly indicated by the blue or black surface, depending on different LiD concentration.

After D plasma exposure, *in situ* NRA was immediately performed on the sample surfaces with 2.5 MeV ^3He beam. The depth profiles indicate that D concentration is around 15–45 at.% in the top 10 μm for most cases, decreasing with depth with a typical e-fold length of approximately 3–30 μm depending on the exposure conditions. An almost pure LiD layer (50 at.%) was found at Li–D co-deposited layer on the clamping ring, implying that Li vapor could easily combine with D atoms or ions to form LiD. A clear increase in D retained in Li with the increasing temperature was found until the temperature reaches ~ 500 °C, which can be explained by the chemical reaction between Li and D atoms using the LiD formation rate constant. When the temperature is high enough and the LiD decomposition pressure is beyond the plasma pressure, LiD dissociation dominates and leads to a decrease in D retained. In order to explain and describe the D retention process and further predict HI inventory in Li, a 1D reaction–diffusion model was built. The modelling D depth profiles can roughly match NRA results and gain total D retained in Li with a given thickness. Both experiments and the model suggest that D is mainly retained in top tens of μm Li layer as the higher the LiD concentration, the lower the D diffusivity, making it difficult for D atoms to diffuse deeper, leading to a deuterium retained fraction below $\sim 2\%$. Either He and H plasma have been applied to remove the retained deuterium in Li and was observed to be relatively effective. After the D-removing shot, the remained deuterium areal density declined to the range of $0.1\text{--}1 \times 10^{22} \text{ D m}^{-2}$ and a high removing efficiency above 96% has been found at temperature above 425 °C.

Acknowledgments

DIFFER is part of the institutes organization of NWO. This work has been carried out within the framework of the EUROfusion Consortium and has received funding from the Euratom research and training programme 2014–2018 and 2020–2024 under Grant Agreement No. 633053. The views and opinions expressed herein do not necessarily reflect those of the

European Commission. We acknowledge the support of the Magnum-PSI Facility Team at DIFFER. The Magnum-PSI facility at DIFFER has been funded by the Netherlands Organisation for Scientific Research (NWO) and EURATOM.

ORCID iDs

W. Ou  <https://orcid.org/0000-0003-2259-7664>

T.W. Morgan  <https://orcid.org/0000-0002-5066-015X>

Reference

- [1] Kallenbach A. *et al* 2013 Impurity seeding for tokamak power exhaust: from present devices via ITER to DEMO *Plasma Phys. Control. Fusion* **55** 124041
- [2] Tobita K. *et al* 2009 Compact DEMO, SlimCS: design progress and issues *Nucl. Fusion* **49** 075029
- [3] Pacher G.W., Pacher H.D., Janeschitz G., Kukushkin A.S., Kotov V. and Reiter D. 2007 Modelling of DEMO core plasma consistent with SOL/divertor simulations for long-pulse scenarios with impurity seeding *Nucl. Fusion* **47** 469–78
- [4] Budaev V.P. *et al* 2017 Tungsten melting and erosion under plasma heat load in tokamak discharges with disruptions *Nucl. Mater. Energy* **12** 418–22
- [5] Philipps V. 2011 Tungsten as material for plasma-facing components in fusion devices *J. Nucl. Mater.* **415** S2
- [6] Pitts R.A. *et al* 2013 A full tungsten divertor for ITER: physics issues and design status *J. Nucl. Mater.* **438** S48–56
- [7] Linke J. *et al* 2011 Performance of different tungsten grades under transient thermal loads *Nucl. Fusion* **51** 073017
- [8] Abdou M.A. *et al* 2001 On the exploration of innovative concepts for fusion chamber technology *Fusion Eng. Des.* **54** 181–247
- [9] Coenen J.W., De Temmerman G., Federici G., Philipps V., Sergienko G., Strohmayer G., Terra A. and Unterberg B. 2014 Liquid metals as alternative solution for the power exhaust of future fusion devices: status and perspective *Phys. Scr.* **T159** 014037
- [10] Morgan T.W., Rindt P., Van Eden G.G., Kvon V., Jaworski M.A. and Cardozo N.J.L. 2018 Liquid metals as a divertor plasma-facing material explored using the Pilot-PSI and Magnum-PSI linear devices *Plasma Phys. Control. Fusion* **60** 014025
- [11] Evtikhin V.A. *et al* 2002 Lithium divertor concept and results of supporting experiments *Plasma Phys. Control. Fusion* **44** 955–77
- [12] Tabarés F.L. 2015 Present status of liquid metal research for a fusion reactor *Plasma Phys. Control. Fusion* **58** 014014
- [13] Hirooka Y., Mazzitelli G., Mirnov S.V., Ono M., Shimada M. and Tabares F.L. 2010 Conference report on the 1st international workshop on Li-applications to boundary control in fusion devices *Nucl. Fusion* **50** 077001
- [14] Mirnov S.V., Azizov E.A., Evtikhin V.A., Lazarev V.B., Lyublinski I.E., Vertkov A.V. and Prokhorov D.Y. 2006 Experiments with lithium limiter on T-11M tokamak and applications of the lithium capillary-pore system in future fusion reactor devices *Plasma Phys. Control. Fusion* **48** 821–37
- [15] Hassanein A., Sizyuk T. and Konkashbaev I. 2009 Integrated simulation of plasma surface interaction during edge localized modes and disruptions: self-consistent approach *J. Nucl. Mater.* **390–391** 777–80
- [16] Van Eden G.G., Morgan T.W., Aussems D.U.B., Van Den Berg M.A., Bystrov K. and Van De Sanden M.C.M. 2016 Self-regulated plasma heat flux mitigation due to liquid Sn vapor shielding *Phys. Rev. Lett.* **116** 135002

- [17] Zuo G.Z. et al 2017 Mitigation of plasma-material interactions via passive Li efflux from the surface of a flowing liquid lithium limiter in EAST *Nucl. Fusion* **57** 046017
- [18] Hogan J.T., Bush C.E. and Skinner C.H. 1997 Lithium effects in plasmas *Nucl. Fusion* **37** 705–11
- [19] Mansfield D.K. et al 1996 Enhancement of tokamak fusion test reactor performance by lithium conditioning *Phys. Plasmas* **3** 1892–7
- [20] Strachan J.D. 1994 Studies of global energy confinement in TFTR supershots *Nucl. Fusion* **34** 1017–38
- [21] Majeski R. et al 2006 Enhanced energy confinement and performance in a low-recycling tokamak *Phys. Rev. Lett.* **97** 075002
- [22] Boyle D.P., Majeski R., Schmitt J.C., Hansen C., Kaita R., Kubota S., Lucia M. and Rognlien T.D. 2017 Observation of flat electron temperature profiles in the lithium tokamak experiment *Phys. Rev. Lett.* **119** 015001
- [23] Sun Z., Hu J.S., Zuo G.Z., Ren J., Cao B., Li J.G. and Mansfield D.K. 2014 Influence of lithium coatings with large-area coverage on EAST plasma performance *Fusion Eng. Des.* **89** 2886–93
- [24] Li J. et al 2013 A long-pulse high-confinement plasma regime in the experimental advanced superconducting tokamak *Nat. Phys.* **9** 817–21
- [25] Erents S.K., McCracken G.M. and Goldsmith P. 1971 Trapping of keV deuterons in lithium *J. Phys. D. Appl. Phys.* **4** 672–6
- [26] de Castro A., Moynihan C., Stemmler S., Szott M. and Ruzic D.N. 2021 Lithium, a path to make fusion energy affordable *Phys. Plasmas* **28** 50901
- [27] Roth J. et al 2008 Tritium inventory in ITER plasma-facing materials and tritium removal procedures *Plasma Phys. Control. Fusion* **50** 103001
- [28] Loureiro J.P.S. et al 2017 Deuterium retention in tin (Sn) and lithium–tin (Li–Sn) samples exposed to ISTTOK plasmas *Nucl. Mater. Energy* **12** 709–13
- [29] Cremona A. et al 2018 Deuterium retention and erosion in liquid Sn samples exposed to D2 and Ar plasmas in GyM device *Nucl. Mater. Energy* **17** 253–8
- [30] Ou W., Al R.S., Vernimmen J.W.M., Brons S., Rindt P. and Morgan T.W. 2020 Deuterium retention in Sn-filled samples exposed to fusion-relevant flux plasmas *Nucl. Fusion* **60** 026008
- [31] Manhard A., Schwarz-Selinger T., Balden M., Dürbeck T., Maier H. and Neu R. 2020 Deuterium retention in solid and liquid tin after low-temperature plasma exposure *Nucl. Fusion* **60** 106007
- [32] Baldwin M.J., Doerner R.P., Luckhardt S.C. and Conn R.W. 2002 Deuterium retention in liquid lithium *Nucl. Fusion* **42** 1318–23
- [33] Martín-Rojo A.B., Oyarzabal E. and Tabarés F.L. 2014 Laboratory studies of H retention and LiH formation in liquid lithium *Fusion Eng. Des.* **89** 2915–8
- [34] Oyarzabal E., Martín-Rojo A.B. and Tabarés F.L. 2015 Laboratory experiments of uptake and release of hydrogen isotopes in liquid lithium *J. Nucl. Mater.* **463** 1173–6
- [35] Capece A.M., Roszell J.P., Skinner C.H. and Koel B.E. 2015 Effects of temperature and surface contamination on D retention in ultrathin Li films on TZM *J. Nucl. Mater.* **463** 1177–80
- [36] De Castro A., Sepetya A., González M. and Tabarés F.L. 2018 Temperature dependence of liquid lithium film formation and deuterium retention on hot W samples studied by LID-QMS. Implications for future fusion reactors *Nucl. Fusion* **58** 046003
- [37] Goldston R.J., Myers R. and Schwartz J. 2016 The lithium vapor box divertor *Phys. Scr.* **014017**
- [38] De Temmerman G. et al 2013 High heat flux capabilities of the Magnum-PSI linear plasma device *Fusion Eng. Des.* **88** 483–7
- [39] van Eck H.J.N. et al 2014 Operational characteristics of the high flux plasma generator Magnum-PSI *Fusion Eng. Des.* **89** 2150–4
- [40] Hubberstey P., Adams P.F., Pulham R.J., Down M.G. and Thunder A.E. 1976 Hydrogen in liquid alkali metals *J. Less-Common Met.* **49** 253–69
- [41] Veleckis E., Yonco R.M. and Maroni V.A. 1977 Solubility of lithium deuteride in liquid lithium *J. Less-Common Met.* **55** 85–92
- [42] Yakimovich K.A. and Biryukova T. 2012 Thermodynamic properties of Li–LiH (LiD, LiT) systems. The phase diagram *Open J. Phys. Chem.* **02** 141–6
- [43] Baldwin M.J., Doerner R.P., Causey R., Luckhardt S.C. and Conn R.W. 2002 Recombination of deuterium atoms on the surface of molten Li–LiD *J. Nucl. Mater.* **306** 15–20
- [44] Hoch M. 1984 The solubility of hydrogen, deuterium and tritium in liquid lead-lithium alloys *J. Nucl. Mater.* **120** 102–12
- [45] Veleckis E. 1979 Decomposition pressures in the ($\alpha + \beta$) fields of the Li–LiH, Li–LiD, and Li–LiT systems *J. Nucl. Mater.* **79** 20–7
- [46] Moriyama H., Iwasaki K. and Ito Y. 1992 Transport of tritium in liquid lithium *J. Nucl. Mater.* **191–194** 190–3
- [47] Chen M., Abrams T., Jaworski M.A. and Carter E.A. 2016 Rock-salt structure lithium deuteride formation in liquid lithium with high-concentrations of deuterium: a first-principles molecular dynamics study *Nucl. Fusion* **56** 1–25
- [48] Abrams T. et al 2016 Suppressed gross erosion of high-temperature lithium via rapid deuterium implantation *Nucl. Fusion* **56** 016022
- [49] Pick M.A. and Sonnenberg K. 1985 A model for atomic hydrogen–metal interactions—application to recycling, recombination and permeation *J. Nucl. Mater.* **131** 208–20
- [50] Gao L., Jacob W., Von Toussaint U., Manhard A., Balden M., Schmid K. and Schwarz-Selinger T. 2017 Deuterium supersaturation in low-energy plasma-loaded tungsten surfaces *Nucl. Fusion* **57** 016026
- [51] Christenson M., Panici D., Moynihan C., Wendeborn J., Anderson J. and Ruzic D.N. 2019 A study on hydrogen absorption and dissolution in liquid lithium *Nucl. Fusion* **59** 026011
- [52] Messer C.E. 1960 *A Survey Report on Lithium Hydride*
- [53] Smith R. and Miser J.W. 1963 Compilation of the Properties of Lithium Hydride *Technical Memorandum E-1302* and NASA-TM-X-483 (<https://ntrs.nasa.gov/citations/19720066808>)
- [54] Jelinek F.J., Tsugawa R.T. and Souers P.C. 1987 Thermal conductivity of pressed lithium hydride and tritide compacts *J. Nucl. Mater.* **144** 290–3
- [55] Morgan T.W. et al 2013 High heat flux capabilities of the Magnum-PSI linear plasma device *Fusion Eng. Des.* **88** 483–7
- [56] Morgan T.W., Balden M., Schwarz-Selinger T., Li Y., Loewenhoff T.H., Wirtz M., Brezinsek S. and De Temmerman G. 2020 ITER monoblock performance under lifetime loading conditions in Magnum-PSI *Phys. Scr.* **T171** 014065
- [57] van Eck H.J.N., Koppers W.R., van Rooij G.J., Goedheer W.J., Engeln R., Schram D.C., Cardozo N.J.L. and Kleyn A.W. 2009 Modeling and experiments on differential

- pumping in linear plasma generators operating at high gas flows *J. Appl. Phys.* **105** 63307
- [58] Rindt P. et al 2019 Using 3D-printed tungsten to optimize liquid metal divertor targets for flow and thermal stresses *Nucl. Fusion* **59** 054001
- [59] Evtikhin V.A., Lyublinski I.E., Vertkov A.V., Belan V.G., Konkashbaev I.K. and Nikandrov L.B. 1999 Calculation and experimental investigation of fusion reactor divertor plate and first wall protection by capillary-pore systems with lithium *J. Nucl. Mater.* **271–272** 396–400
- [60] Rindt P., Morgan T.W., Van Eden G.G., Jaworski M.A. and Lopes Cardozo N.J. 2019 Power handling and vapor shielding of pre-filled lithium divertor targets in Magnum-PSI *Nucl. Fusion* **59** 056003
- [61] Pricshivichin A.S., Krat S.A., Harina A.P. and Picarev A.A. 2019 The dependence of lithium emissivity from temperature in vacuum *Probl. At. Sci. Technol. Ser. Thermonucl. Fusion* **42** 89–95
- [62] Mayer M. 1997 *SIMNRA User's Guide* (Germany: Garching)
- [63] Chandra R., de Blank H.J., Diomede P., van Eck H.J.N., van der Meiden H.J., Morgan T.W., Vernimmen J.W.M. and Westerhof E. 2021 B2 5-Eunomia simulations of Magnum-PSI detachment experiments: I. Quantitative comparisons with experimental measurements *Plasma Phys. Control. Fusion* **63** 095006
- [64] Christenson M., Moynihan C. and Ruzic D.N. 2018 A distillation column for hydrogen isotope removal from liquid lithium *Fusion Eng. Des.* **135** 81–7